Coastal Engineering 182 (2023) 104302

Contents lists available at ScienceDirect

Coastal Engineering

journal homepage: www.elsevier.com/locate/coastaleng

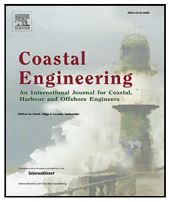

Wave impact on rigid and flexible plates

Tommaso Attili [a,*], Valentin Heller [a], Savvas Triantafyllou [b]

[a] Environmental Fluid Mechanics and Geoprocesses Research Group, Faculty of Engineering, University of Nottingham, Nottingham NG7 2RD, UK
[b] Institute for Structural Analysis and Aseismic Research, School of Civil Engineering, National Technical University of Athens, Athens, Greece

ARTICLE INFO

Keywords:
Coastal structures
Flexible plates
Laboratory tests
Numerical modelling
Wave-structure interaction

ABSTRACT

Wave impact on offshore and coastal structures, such as oil and gas rigs, offshore wind turbine platforms, breakwaters, flood protection systems and wave energy converters, involve complex wave-structure interactions. These interactions are particularly challenging for flexible structures and may result in structural damage in extreme cases. Some studies found reduced wave forces on flexible compared to rigid walls. However, the technical literature includes inconclusive results on this aspect and an accurate understanding of wave-structure interaction is still lacking. The present study comprehensively investigates wave-structure interaction with the numerical toolbox solids4foam to resolve this shortcoming. The numerical pressures, forces and plate deformations have been successfully validated with new and already available laboratory experiments, e.g. the numerical plate displacement deviates less than 35% from the laboratory observation. 117 two-dimensional (2D) tests of waves impacting plates of different stiffnesses located in the open sea (offshore) and on the coast (onshore) were then conducted, complemented with 2 three-dimensional (3D) tests with offshore plates. For most of the offshore and onshore tests, the plate stiffness had a negligible effect on the upwave force. However, for the most flexible offshore plates, the downwave water depth increased due to plate deformation, resulting in up to 40% smaller total forces on the flexible than the rigid plates. This was also confirmed in the 3D tests. The response of the offshore plates was then successfully examined in view of the Euler–Bernoulli beam theory. In the onshore tests, the wave force showed two peaks confirming previous observations. The second force peak was up to 3.3 times larger than the first one, with the rigid plates not necessarily resulting in the largest peaks. New semi-theoretical correlations to predict wave forces on onshore plates are finally suggested, as a simple function of the offshore wave energy. Such findings enhance the physical understanding of wave-structure interaction and are aimed at supporting the design of coastal and offshore structures.

1. Introduction

1.1. Background

Waves pose a challenge for a range of coastal structures. These include oil and gas rigs, offshore wind turbine platforms, breakwaters, flood protection systems and Wave Energy Converters (WECs). Such structures may experience significant deformations under wave loading leading to a mutual interplay between the waves and the structure, referred to as Wave-Structure Interaction (WSI). WSI resulted in structural damage and even failure in extreme cases. For example, an offshore platform in the Gulf of Mexico collapsed during the 2002 hurricane Lili (Moan, 2018) and the Dawlish seawall breached in 2014 due to a severe storm (Dawson et al., 2016).

Analytical, laboratory and numerical modelling of WSI traditionally addressed rigid structures (Sainflou, 1928; Cross, 1967; Mallayachari and Sundar, 1995; Higuera et al., 2014; Attili et al., 2021). Nevertheless, recent applications, e.g. the use of deformable materials for WECs (Chaplin et al., 2012; Collins et al., 2021) and vegetation for shore protection (van Veelen et al., 2021), raised the need to model the structure as flexible, making WSI even more significant.

Some researchers (Linton et al., 2013; Rao et al., 2017; Zhang et al., 2019) observed benefits, e.g. reduced wave forces, when a deformable rather than a rigid wall is used. A few studies (Laya et al., 1984; Yuan and Huang, 2015) suggested reduction terms in the Morison equation (Morison et al., 1950), providing wave loading on stationary rigid cylinders, if the cylinders are moving. This opens up promising potential solutions by partially or fully replacing rigid coastal structures with flexible ones. However, current studies are still inconclusive; elastic walls showed larger wave pressures and forces under certain conditions compared to rigid ones (Mai et al., 2020).

An accurate understanding of the plate flexibility effect on wave loading is still a major challenge and an exhaustive analysis involving rigid and flexible structures is lacking. The present study focuses on an

* Corresponding author.
E-mail addresses: tommaso.attili@nottingham.ac.uk (T. Attili), valentin.heller@nottingham.ac.uk (V. Heller), savtri@mail.ntua.gr (S. Triantafyllou).

https://doi.org/10.1016/j.coastaleng.2023.104302
Received 6 December 2022; Received in revised form 7 March 2023; Accepted 19 March 2023
Available online 23 March 2023

extensive investigation of WSI mimicking a range of real applications. This relies on numerical modelling of waves impacting rigid and flexible plates, located either offshore or onshore, using an available toolbox in foam-extend 4.0 (FE 4.0).

1.2. Previous work

1.2.1. Laboratory studies

Most laboratory studies of WSI have been conducted for the validation of numerical models. The most relevant benchmark cases include dam break waves involving elastic gates (Antoci et al., 2007), waves impacting rigid and flexible walls (Kimmoun et al., 2009; Linton et al., 2013; Didier et al., 2014) and dam break waves impacting flexible obstacles (Liao et al., 2015).

Kimmoun et al. (2009) conducted laboratory experiments of solitary waves impacting a flexible plate. Wave breaking was initiated in proximity of the plate in most tests, resulting in a complex wave-plate interaction. The wave-plate impact and the plate deflection were recorded, establishing a new database for numerical validation. Linton et al. (2013) conducted large-scale experiments in a 104 m long, 3.66 m wide and 4.57 m deep flume to investigate tsunamis impacting timber walls. The most flexible wall experienced smaller forces compared to stiffer walls. The measured peak forces were in good agreement with the equation (Cross, 1967)

$$F_I = \frac{1}{2}\rho_w g h_s^2 + C_f \rho_w h_s \bar{u}_s^2, \tag{1}$$

predicting the force on a vertical and rigid wall due to a surge, where ρ_w is the water (subscript w) density, g the gravitational acceleration, h_s the shore (subscript s) water depth, $\bar{u}_s$ the depth-averaged velocity and C_f is a force coefficient related to the inclination of the free water surface.

Mai et al. (2020) experimentally investigated the effects of the structural elasticity during wave impacts on a vertical plate and vertically falling plate impact onto a water surface. In both cases, the structural elasticity had an effect on the impact load. Reduced forces and pressures were observed in the slamming tests for the elastic plates compared to rigid ones at high impact velocities only. The wave loading on the flexible plates was smaller than on the rigid plate under certain conditions, namely for high aeration waves. For slightly breaking waves, however, the elastic plates showed larger pressures and forces.

Large-scale laboratory tests have been conducted by Krautwald et al. (2022) to analyse the failure of rigid and elasto-plastic buildings under extreme wave loadings. These involved waves transforming into bores and impacting onshore buildings. For small wave heights, the structure stiffness had a negligible effect on the measured forces. For increasing wave heights, the elasto-plastic structures showed less pronounced force peaks compared to rigid ones. However, the forces were similar for both structures during the second stage of the impact, with the deformable structure experiencing even larger forces in some cases.

To the best of the authors' knowledge, a comprehensive benchmark case for wave impact on flexible structures is still lacking. This should provide the wave parameters, e.g. water surface elevation, pressure and force, as well as the plate displacement and/or deformation. In addition, the effect of the structure elasticity on the wave force is still uncertain requiring further study.

1.2.2. Numerical modelling

Given the maturity of Computational Fluid Dynamics (CFD) and Computational Structural Dynamics (CSD), numerical modelling has been increasingly applied to WSI phenomena (Liu and Zhang, 2019). Both mesh-based, e.g. the Finite Volume Method (FVM, Tuković et al., 2018), and mesh-free, e.g. Smoothed Particle Hydrodynamics (SPH, Didier et al., 2014), methods have been successfully applied with either monolithic (Rao et al., 2017; Liu and Zhang, 2019) or partitioned (Sotiropoulos and Yang, 2014) coupling approaches. In the monolithic approaches the fluid and solid governing equations are solved within a single solver. On the other hand, partitioned techniques individually solve the fluid and solid domains with an exchange of information at the fluid-solid interface.

Mesh-based methods are highly reliable for both CFD and CSD and also computationally efficient. However, they may become inaccurate for large deformations. He and Kashiwagi (2012) proposed a mixed Eulerian Lagrangian method monolithically coupled with a Finite Element Method (FEM). Solitary waves impacting elastic plates were investigated, showing that the hydroelastic behaviour strongly depends on the plate stiffness. Several models have been developed in the OpenFOAM (OF) framework (Higuera et al., 2013; Chen et al., 2014; Higuera et al., 2014; Hu et al., 2016; Rege and Hjertager, 2017; Tuković et al., 2018; Cardiff et al., 2018; Chen et al., 2019; Chen et al., 2020; Romano et al., 2020; Di Paolo et al., 2021; Hu et al., 2022), showing a great potential in tackling WSI phenomena (Huang et al., 2022).

Mesh-free approaches typically handle moving interfaces and large deformations more efficiently than mesh-based methods. However, they show instabilities and inaccuracies in the structural stresses (Liu and Zhang, 2019) and are more computationally expensive (Kumar et al., 2015). New developments in the SPH method have been presented by Antoci et al. (2007), Didier et al. (2014), Huang et al. (2018), Khayyer et al. (2018), Sun et al. (2019) and O'Connor and Rogers (2021). These have been validated with benchmark cases such as dam break waves involving an elastic gate (Antoci et al., 2007), a wave impacting an offshore wall (Didier et al., 2014) and a dam break wave impacting a flexible obstacle (Liao et al., 2015). Overall, SPH models showed the capability of capturing the physics of WSI phenomena, with some deviations related to the structural response in most cases (Antoci et al., 2007; Sun et al., 2019; O'Connor and Rogers, 2021).

Mesh-based and mesh-free methods have eventually been coupled to combine their strengths. In these hybrid approaches, however, the fluid-solid coupling is even more challenging. This concerns particularly the energy balance at the interface (Degroote, 2013). Kumar et al. (2015) developed an SPH-FVM model within the OF framework, showing a good agreement for a dam break experiment. However, the solid analysis was not provided. A Moving Particle Semi-implicit (MPS, Khayyer et al., 2019) method was coupled with FEM by Rao et al. (2017). This approach was used to investigate solitary waves impacting rigid and flexible plates. Results showed larger pressures acting on the rigid than on the elastic plates. Zhang et al. (2019) proposed a coupled MPS-FEM approach to investigate regular waves interacting with a horizontal plate. Comparisons with laboratory observations indicated the capability of this approach to accurately solve WSI phenomena.

The open source software OF is robust, stable and supports two-phase flows with a range of turbulence models and wave theories. Given the reliability and flexibility of the OF models, the available toolbox solids4foam (Cardiff et al., 2018) was used in the present study. This toolbox is capable of modelling both the fluid and structure with a partitioned coupling (Section 2). This numerical model has already been successfully applied to fluid-solid interaction phenomena (Mohammadi et al., 2021; Girfoglio et al., 2021). However, further validation is required, being one of the shortcomings addressed in the present study.

1.3. Aims and structure

The present study is aimed at:

- Validating the numerical model solids4foam with new laboratory experiments and the one from Kimmoun et al. (2009).
- Providing new physical insight into linear and solitary waves impacting plates of different stiffnesses and inclinations located in the open sea (offshore).
- Providing new physical insight into broken solitary waves impacting plates of different stiffnesses located on the coast (onshore).

The remainder of this article is organised as follows. The numerical model is presented in Section 2 along with the numerical set-ups and the test programme. The laboratory experiments are discussed in Section 3. Section 4 includes the validation of the numerical toolbox along with the numerical wave forces and plate responses for the offshore and onshore tests. In Section 5, the results are discussed and compared with existing prediction methods. The main conclusions are then summarised in Section 6. The appendices include the convergence tests (Appendix A), the Euler-Bernoulli beam theory for the offshore tests (Appendix B) and new correlations for the onshore plate displacements and stresses (Appendix C).

2. Numerical model

The numerical investigation was conducted with the open source toolbox solids4foam (Cardiff et al., 2018) implemented in FE 4.0 (OpenFOAM extension, 2016). This toolbox solves fluid-solid interaction phenomena employing the FVM discretisation for both domains and with a partitioned coupling approach.

2.1. Governing equations and coupling method

The fluid was modelled as an incompressible Newtonian fluid satisfying the continuity and the Reynolds-Averaged Navier-Stokes (RANS) equations

$$\nabla \cdot \bar{\mathbf{u}} = 0 \tag{2}$$

$$\frac{\rho \partial \bar{\mathbf{u}}}{\partial t} + \rho(\bar{\mathbf{u}} \cdot \nabla)\bar{\mathbf{u}} = -\nabla \bar{p} + \rho \nabla \cdot (\mu \nabla \cdot \bar{\mathbf{u}} - \overline{\mathbf{u}'\mathbf{u}'}) + \rho \mathbf{g} + f_\sigma, \tag{3}$$

where $\bar{\mathbf{u}} = (\bar{u}_x, \bar{u}_y, \bar{u}_z)$ is the mean fluid velocity vector, $\bar{p}$ the mean pressure, ρ the fluid density, μ the fluid dynamic viscosity, $\overline{\mathbf{u}'\mathbf{u}'}$ the turbulent stress tensor, t the time, $\mathbf{g}$ the gravitational acceleration vector and f_σ the surface tension force per unit volume (Brackbill et al., 1992). The tensor $\overline{\mathbf{u}'\mathbf{u}'}$ is defined according to the turbulence model considered (Ferziger, 1987; Jasak, 1996). The k-ε model (Launder and Spalding, 1974) has been used herein. This standard model ensures fast convergence and reliability in modelling fully-turbulent processes.

Eqs. (2) and (3) were discretised into a set of algebraic equations and solved with the PIMPLE loop (Aguerre et al., 2013). The Courant-Friedrichs-Lewy (CFL) convergence condition (Courant et al., 1928)

$$C = \frac{\bar{u}_x \Delta t}{\Delta x} + \frac{\bar{u}_y \Delta t}{\Delta y} + \frac{\bar{u}_z \Delta t}{\Delta z} \leq 1 \tag{4}$$

was used to control the time integration. In Eq. (4), C is the Courant number and Δx, Δy and Δz are the cell sizes in the x, y and z direction, respectively. The initial time step Δt was dynamically adapted to satisfy the CFL condition throughout the simulation, with the mean C typically not exceeding 0.012.

The water-air flows herein were solved by employing the Volume Of Fluid (VOF) method (Hirt and Nichols, 1981) with the fraction of volume α; α varies from 0 to 1, with $\alpha = 0$ denoting air (subscript a), $\alpha = 1$ water and $0 < \alpha < 1$ the air-water interface. In the present study, $\alpha = 0.5$ was used to track the water surface. The physical properties ρ and μ are computed as

$$\rho = \rho_w \alpha + \rho_a (1 - \alpha) \tag{5}$$

$$\mu = \mu_w \alpha + \mu_a (1 - \alpha). \tag{6}$$

Once Eqs. (2) and (3) were solved, α was updated based on the transport equation

$$\frac{\partial \alpha}{\partial t} + \nabla \cdot (\bar{\mathbf{u}}\alpha) + \nabla \cdot [\alpha(1 - \alpha)\mathbf{u}_r] = 0. \tag{7}$$

The compression term $\nabla \cdot [\alpha(1 - \alpha)\mathbf{u}_r]$, where $\mathbf{u}_r$ is the compression velocity vector, was introduced by Weller et al. (1998) to reduce the numerical diffusion.

The waves were generated with the toolbox waves2Foam (Jacobsen et al., 2012). The wave generation was based on the relaxation zone technique, consisting of a relaxation function applied to evaluate $\bar{\mathbf{u}}$ and α inside the relaxation zone (Jacobsen et al., 2012). A relaxation zone of 3 times the wave length L was used in all tests of the present study (Fig. 1a).

A Lagrangian approach was adopted for the solid domain. In the present study, large displacement kinematics were considered along with the Neo-Hookean elastic constitutive law. The momentum equation is

$$\rho_s \frac{\partial^2 \mathbf{d}_s}{\partial t^2} + \nabla \cdot [(J \mathbf{D}_F^{-T}) \cdot \boldsymbol{\sigma}_s] = \rho_s \mathbf{g}, \tag{8}$$

where $\mathbf{d}_s$ is the solid (subscript s) displacement vector, ρ_s the solid density, $\mathbf{D}_F = \mathrm{I} + (\nabla \mathbf{d}_s)^T$ the deformation gradient, with the identity matrix I, J the determinant of $\mathbf{D}_F$ and $\boldsymbol{\sigma}_s$ the stress tensor in Voigt notation.

The fluid-solid coupling was performed through a partitioned approach. The fluid domain was solved with a Dirichlet condition for the mean velocity vector $\bar{\mathbf{u}}$ at the interface and the solid with a stress boundary condition (Cardiff et al., 2018). For each time step, the fluid velocity and pressure fields were updated with Eqs. (2) and (3) through the PIMPLE loop (Aguerre et al., 2013), and Eq. (7) was solved to track the water-air interface. Thereafter, the fluid forces acting on the solid were evaluated and applied to the solid interface. The traction Neumann condition was employed at the solid interface, where the boundary condition for the displacement was set as "solidTraction" (Cardiff et al., 2018). The solid domain was solved, then the new solid velocities were transferred to the fluid using an under-relaxation technique (Cardiff et al., 2018). This involved multiplying the new solid velocities by a relaxation factor ≤ 1 to optimise the numerical convergence. Consequently, the fluid mesh was updated and the loop was performed until convergence was achieved.

2.2. Numerical set-up and test programme

Linear and solitary waves impacting plates located either offshore or onshore were investigated with the 2D set-ups shown in Fig. 1. These idealised wave types represent a range of real-world applications, from wind waves to more extreme cases such as tsunamis. In the offshore tests, the plate was located $4L$ from the upstream boundary of the flume (Fig. 1a). The plate, with a height $l = 30$ m and thickness $s = 2$ m, was fixed on a substructure with height $l_s = 35$ m and submerged by 25, 50 or 75% of l. This design is related to the concepts of the MOSE mobile gate (Erbisti, 2014) and Oyster WEC (Lagoun et al., 2010).

Young's moduli $E = 1, 30$ and 1000 GPa were used, modelling extreme scenarios of real applications, with $E = 1$ GPa representing a variety of plastics and $E = 1000$ GPa as an upper bound for rigid plates. Inclinations of the plate $\beta = 60, 75$ and 90° were investigated. Linear and solitary waves with various wave amplitudes a, heights H and periods T were simulated within a total of 72 tests (Table 1). A resolution of $\Delta x = \Delta z = 0.15$ m in a 25.00 m × 32.00 m refined area (Appendix A) was employed, with $\Delta x = \Delta z = 0.60$ m in the remainder of the domain (Fig. 1a).

In the onshore tests, the plate was located on the horizontal section of the shore at a distance of $L_s = 4$ m from the transition point (Fig. 1b). An inclination of the shore of $\beta_s = 30°$ was used, as a typical value for the friction angle of sand. Water depths of $h = 2$, 3 and 4 m were investigated, resulting in freeboards of $z_f = 0, 1$ and 2 m. For each wave condition, 5 plates with different E, boundary conditions and thicknesses were used (Table 2), resulting in a total of 45 tests. For the Rigid (R) and "Top Free" (TF) cases the plate was fixed to the foundation and the top end was free to move. In the "Roller Support" (RS) case the plate was fixed to the foundation and the horizontal displacement d_x at the top end was prevented. The fundamental natural

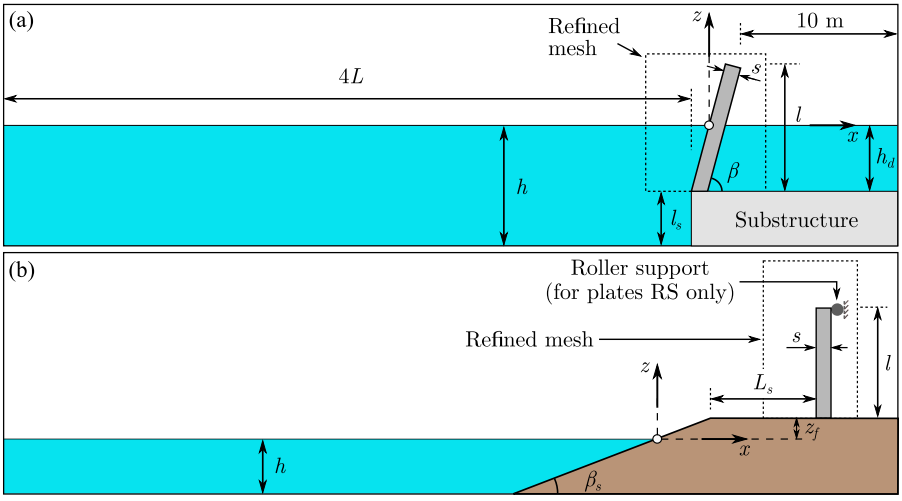

Fig. 1. Side views of the numerical set-ups: (a) offshore and (b) onshore.

Table 1
Test programme for the 2D numerical tests.

Parameter	Symbol	Unit	Offshore	Onshore
Water depth	h	m	42.5, 50.0, 57.5	2, 3, 4
Plate height	l	m	30	3
Plate inclination	β	°	60, 75, 90	90
Young's modulus	E	GPa	1, 30, 1000	1, 1000
Plate thickness	s	m	2	0.15, 0.30
Dimensionless rigidity	$Es^3/(12\rho_w g h^4)$	–	0.006 to 20.830	0.112 to 1.433 × 10^4
Plate density	ρ_s	kg/m^3	1500, 8000	1500, 8000
Plate boundary condition	–	–	Top free	Top free, roller support
Shore freeboard	z_f	m	–	0, 1, 2
Shore length	L_s	m	–	4
Shore inclination	β_s	°	–	30
Linear waves	H	m	2.62 to 3.55	–
	H/h	–	0.046 to 0.080	–
	T	s	6, 8, 10	–
	$T(g/h)^{0.5}$	–	2.48 to 3.84	–
Solitary waves	a	m	3.56 to 3.75	0.9, 1.2, 1.5
	a/h	–	0.06 to 0.09	0.225 to 0.750
Number of tests	–	–	72	45

Table 2
Classification of the 5 plates used in the onshore tests.

Notation	E (GPa)	ρ_s (kg/m^3)	s (m)	Boundary condition	f_s (Hz)
R	1000	8000	0.30	Top free	60.20
RS1	1	1500	0.30	Roller support	–
RS2	1	1500	0.15	Roller support	–
TF1	1	1500	0.30	Top free	4.40
TF2	1	1500	0.15	Top free	2.20

frequency f_s of the plates R, TF1 and TF2 (Table 2) was computed as (Gibson, 2007)

$$f_s = \frac{(1.875)^2}{2\pi l^2}\sqrt{\frac{Es^2}{12\rho_s}}. \tag{9}$$

A resolution of $\Delta x = \Delta z = 0.0250$ m, with $\Delta x = \Delta z = 0.0125$ m in a 1.40 m × 3.00 m refined area, was used (Fig. 1b).

The simulations were run on the High Performance Computing (HPC) cluster Augusta at the University of Nottingham using 40 Central Processing Units (CPUs) and 150 GB of memory. In the offshore layout (≈0.1 million cells), the solitary wave tests took up to approximately 10 h to simulate 30 to 33 s and linear wave tests took 34 h for a simulation time of 110 s. Onshore tests (≈0.5 million cells) required up to 20 h to simulate 6 to 10 s.

2.3. 3D simulations

3D simulations have been conducted with the 15 m wide wave flume shown in Fig. 2. The plate, with the same width as the flume, was 30 m high with $s = 0.30$ m and supported at both ends. A volume of water with depth $h_d = 15$ m was retained downwave (subscript d) of this plate. This scenario mimics a section of the hull of a Floating Production Storage and Offloading (FPSO) unit.

The simulations involved flexible and rigid plates with $E = 2 \cdot 10^2$ and $2 \cdot 10^4$ GPa, respectively, impacted by a solitary wave with $a/h = 0.07$. The density of the plate was $\rho_s = 8000$ kg/m^3 in both cases. A resolution of $\Delta x = \Delta y = \Delta z = 0.15$ m was used in a 30.00 m × 15.00 m × 30.00 m refined volume, with $\Delta x = \Delta y = \Delta z = 0.60$ m in the remainder of the domain resulting in ≈6 million cells. The numerical tank boundaries at $y = -7.5$ and 7.5 m were modelled as smooth walls. The simulations were again run on Augusta using 40 CPUs and 120 GB of memory. The rigid plate test took approximately 28 h and the flexible case 150 h to simulate 30 s.

3. Physical model

Laboratory experiments were conducted in an approximately 15 m long, 0.245 m wide and 0.460 m deep flume, as shown in Fig. 3a. Cartesian coordinates (x, y, z) are used in this study, with the origin at the still water surface. The tests involved linear and solitary waves

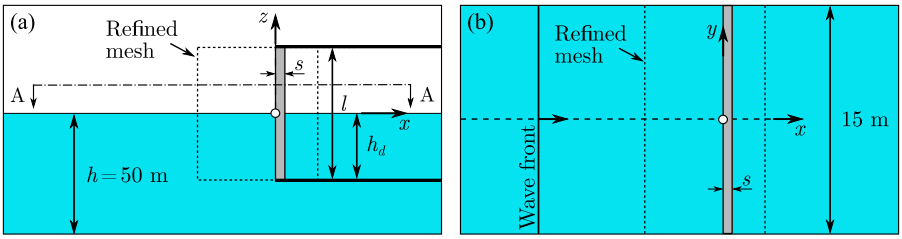

Fig. 2. 3D simulations: (a) lateral view and (b) section AA of the 3D numerical set-up with the hull of a FPSO unit.

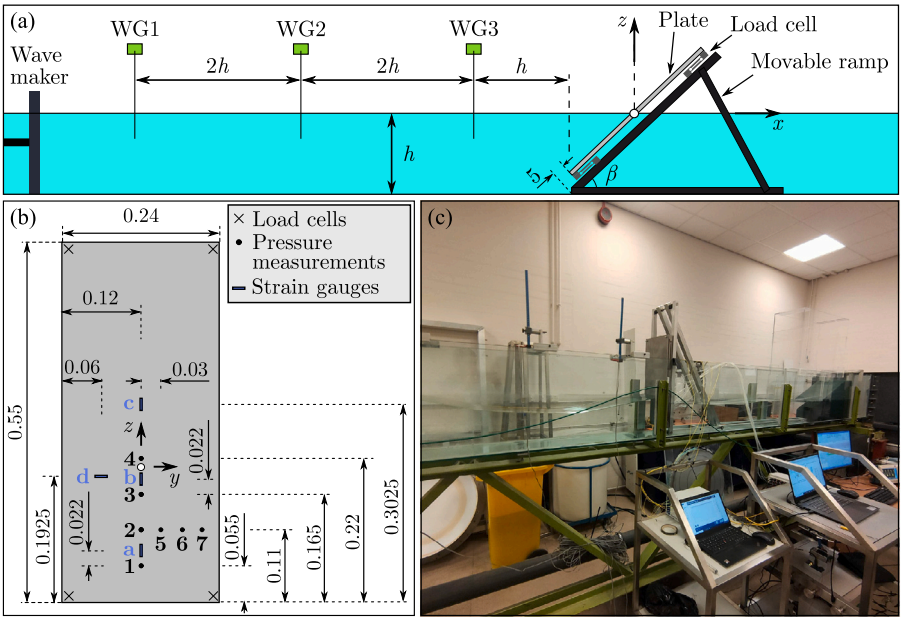

Fig. 3. Experimental set-up: (a) side view of the wave flume and plate, (b) frontal view of the plate (dimensions in m) and (c) overview of the flume with the instrumentation.

impacting a 0.55 m × 0.24 m plate. The flume was equipped with a piston-type wave maker. The plate was located 11.43 m downwave the wave maker and supported by a movable angled ramp, enabling several plate inclinations β. A gap of 2.0 to 2.5 mm between the plate and the lateral walls of the flume allowed for a free movement of the plate. A 4 mm thick acrylic (Young's modulus E = 3.30 GPa) and a 3 mm thick stainless steel plate (E = 200 GPa) were used in the tests to model flexible and rigid structures.

The water surface elevations were recorded at 3 locations with resistance-type Wave Gauges (WGs, Fig. 3a). They recorded at 100 Hz with an accuracy of ±1 mm. An array of MPXV5004GC7U (RS Components UK) Precision Pressure Transducers (PPTs) was used to measure the water pressure at the plate. Each PPT was attached to the lateral wall of the flume and connected with a water-filled pipe to the plate. The locations of the pressure measurements is shown in Fig. 3b. The PPTs sampled at 100 Hz with an estimated accuracy of ±10 Pa. Both the WGs and PPTs were calibrated daily by changing the still water levels.

Load Cells (LCs) have been manufactured in-house to measure the wave forces on the plates. These consisted of stainless steel S beams equipped with fibre optic strain gauges and the data were interrogated with a FS22SI BraggMETER. The 4 LCs were located at the corners of the plate and fixed to the movable angled ramp (Fig. 3a). They have been individually calibrated resulting in an overall accuracy of ±0.3 N. The force was recorded at 1 kHz. In addition, KFWB Series Waterproof Strain Gauges (SGs) were mounted on both the upwave and downwave sides of the acrylic plate to measure deflections (Fig. 3b). They recorded at 100 Hz with an accuracy of $\pm 10^{-6}$.

Table 3
Main parameters in the validation with 2 laboratory experiments.

Experiment	h (m)	a (m)	s (m)	E (GPa)	ρ_s (kg/m^3)	β (°)
1	0.250	0.064*	0.003	200.000	8000	90
2	0.250	0.064*	0.004	3.300	1200	90

*Values were observed at WG1 in tests conducted without the plate.

4. Results

4.1. Offshore

4.1.1. Validation of solids4foam with new laboratory experiments

The validation of solids4foam for rigid plates was addressed in Attili et al. (2021). The numerical model for flexible plates is validated herein with 2 new laboratory experiments (Section 3) of solitary waves impacting a stainless steel and a plastic plate. An overview of the main experimental parameters is given in Table 3. The numerical set-up consisted of a 3D wave flume mimicking one half (0.00 m ≤ y ≤ 0.12 m) of the experimental flume given the symmetry of the wave field and plate. Small strains were considered for the plates in these simulations with the linear elastic constitutive law.

To accurately model the dynamics of the acrylic plate by reducing computational cost, a plate with s = 0.008 m, E = 412.5 MPa and ρ_s = 600 kg/m^3 was used in the simulation. This has the same flexural rigidity EI and natural period T_s as the laboratory plate where I is the moment of inertia. A mesh resolution of $\Delta x = \Delta y = \Delta z$ = 0.0040 m was used for the fluid domain in both experiments and $\Delta x = \Delta y = \Delta z$ =

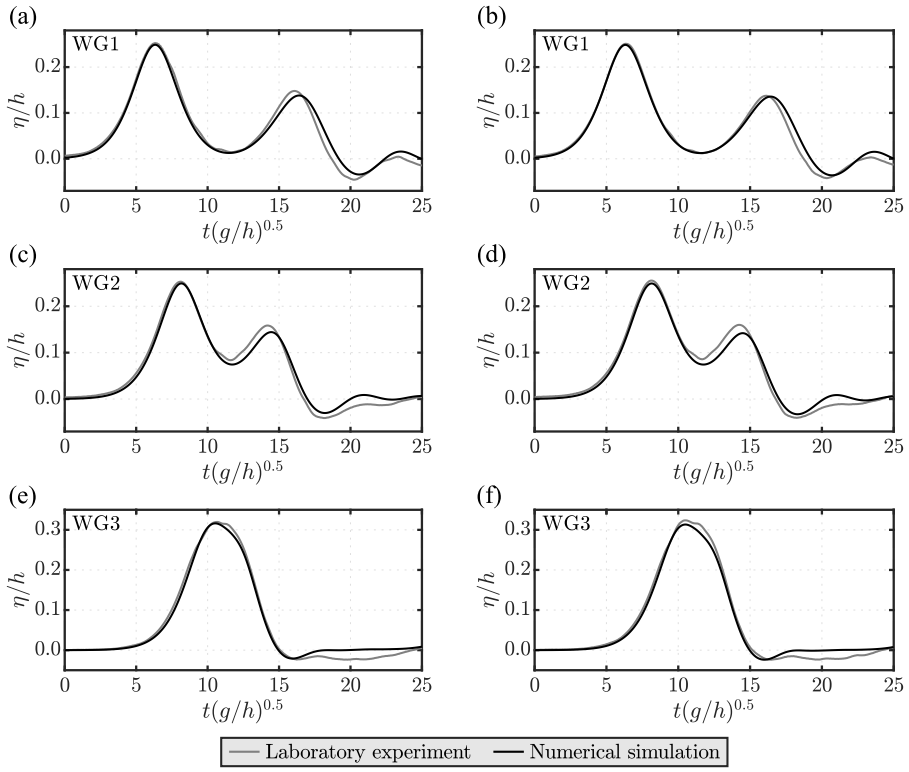

Fig. 4. Comparison of the experimental and numerical water surface elevations η/h at all 3 WGs for experiment 1 (a, c, e) and 2 (b, d, f) of Table 3.

0.0015 m and $\Delta x = \Delta y = \Delta z = 0.0020$ m were employed for the solid domain in experiment 1 and 2, respectively.

The relative water surface elevations η/h observed at the 3 WGs (Fig. 3a) are shown in Fig. 4 for both experiments. The wave travelled along the flume, impacted the plate and was reflected. During wave impact, vibrations of the pipes connecting the PPTs were observed in the laboratory tests. As a result, oscillations of the pressure p, which are not directly related to wave pressures, were observed, as shown in Fig. 5. However, as also revealed by low-pass filter analyses, these oscillations follow the overall trend of the wave pressure such that these measurements are still valuable. In the end, the laboratory measurements were not low-pass filtered to avoid attenuating significant high frequencies due to plate vibrations.

The comparison between laboratory and numerical results shows a good agreement for η/h and $p/(\rho_w g h)$ (Figs. 4 and 5a, b, c, d). The incident and reflected waves, as well as their superposition, are well captured by the numerical model with less than 12% deviations. The numerical (subscript *num*) p_{num} at PPT1, 2, 3 and 6 shows similar trends as the experimental (subscript *exp*) p_{exp}, apart from the previously mentioned oscillations. The normalised root mean square error was computed as

$$nRMSE = \frac{\sqrt{\frac{1}{\mathrm{N}}\sum_{\mathrm{i}}^{\mathrm{N}}\left(p_{num,\mathrm{i}} - p_{exp,\mathrm{i}}\right)^2}}{\left(p_{exp,max} - p_{exp,min}\right)}, \tag{10}$$

where N is the number of the considered p values and the subscripts *max* and *min* stand for the maximum and minimum values.

Deviations of less than 7.6% were observed for p_{exp} across the plate between PPT2, 5, 6 and 7 in experiment 1. This was confirmed by the numerical results, where p_{num} showed negligible deviations (<1%) between $y = 0.00$ m and $y = 0.10$ m. However, reduced p_{num} were observed in proximity of the plate sides as a result of larger velocities due to the gaps between the plate and the flume walls. This effect induced 24.5% smaller p_{num} at $y = 0.12$ m than at $y = 0$ m. Similar results were observed in experiment 2.

The 3D experimental and numerical total forces $F_{3D} = F_{3D,u} - F_{3D,d}$, where $F_{3D,u}$ is the upwave (subscript u) and $F_{3D,d}$ the downwave force, are compared in Fig. 5e, f. The force is overestimated by the numerical simulations by up to 18 and 33% for experiment 1 and 2, respectively. These deviations may be explained by the inability of the numerical model to fully capture the 3D effects due to the lateral gaps. The numerical simulations tend to overpredict the laboratory p in proximity of the gaps, as indicated by the comparison at PPT7, resulting in larger F_{3D} on the plate.

Fig. 6 shows the numerical and experimental strain ϵ_{zz} at the upwave SGb and SGc (Fig. 3b) for experiment 2. The largest deformations of the plate were observed at SGb followed by SGc. This behaviour is captured in the numerical simulation, however, with up to 45.2 and 59.7% deviations for SGb and SGc. The overestimation of the wave force in combination with the absence of physical damping in solids4foam (Section 4.2.1) may explain the observed deviations. To sum up, the validation of solid4foam with new laboratory tests showed its capability of capturing the water surface elevation and the wave pressures well, however, it overestimates the wave forces and plate deformation.

4.1.2. A numerical representative test

Fig. 7 shows an offshore test with wave impact and reflection. In the present study, $t = 0.0$ s is the instant when the wave front reaches the plate. The horizontal (subscript H) relative forces acting on a rigid and flexible plate with $E = 1000$ and 1 GPa, respectively, for a linear wave with $a/h = 0.038$ and $T(g/h)^{0.5} = 3.54$, are shown in Fig. 8a.

Both the force acting on the upwave side of the plate $F_{H,u}$ and the total force $F_H = F_{H,u} - F_{H,d}$ due to the hydrostatic and wave pressures are shown in Fig. 8a. The stiffness of the plate results in negligible deviations of $F_{H,u}/(\rho_w g h^2)$. On the other hand, slightly larger deviations, of up to 6%, are observed for $F_H/(\rho_w g h^2)$. These are due to the increase in the downwave water depth h_d for the flexible plates. The time series of the relative d_x/l are shown in Fig. 8b.

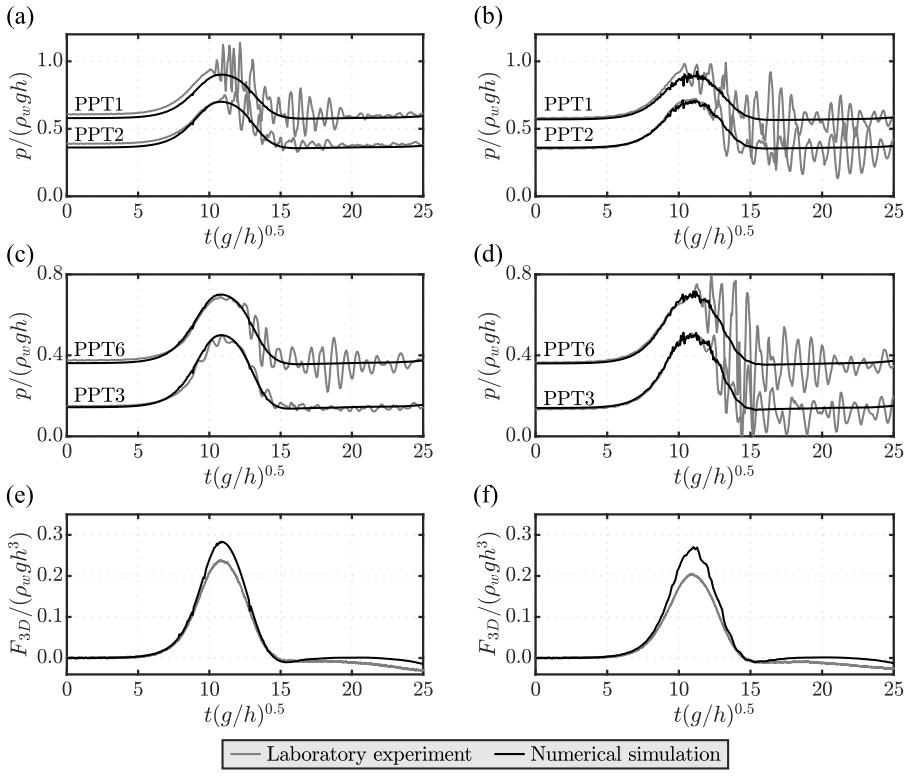

Fig. 5. Comparison of the experimental and numerical pressures $p/(\rho_w gh)$ at (a) PPT1 ($nRMSE = 0.097$) and 2 ($nRMSE = 0.085$), (c) 3 ($nRMSE = 0.041$) and 6 ($nRMSE = 0.078$) and (e) force $F_{3D}/(\rho_w gh^3)$ for experiment 1 and $p/(\rho_w gh)$ at (b) PPT1 ($nRMSE = 0.108$) and 2 ($nRMSE = 0.115$), (d) 3 ($nRMSE = 0.094$) and 6 ($nRMSE = 0.102$) and (f) $F_{3D}/(\rho_w gh^3)$ for experiment 2 of Table 3.

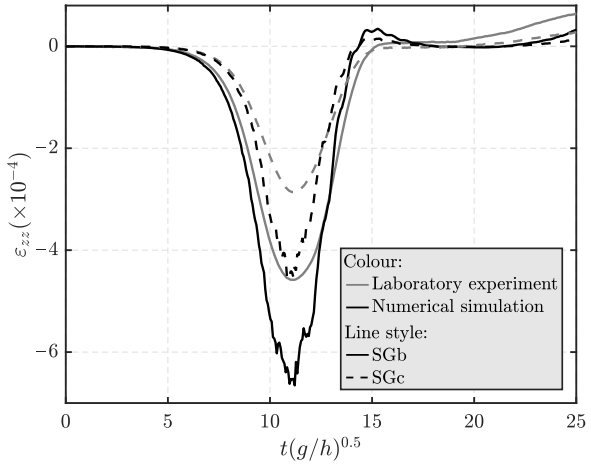

Fig. 6. Comparison of the experimental and numerical strains ϵ_{zz} at SGb and SGc for experiment 2 of Table 3.

4.1.3. Numerical run-up and force

The maximum dimensionless run-up heights R/h are shown in Fig. 9a versus a/h for the linear and solitary wave tests. Overall, R/h increases with increasing a/h, following a linear trend in the solitary wave tests. The most deformable plates show slightly smaller R/h with delays compared to the rigid plates, however, with small deviations. The numerical R_{num}/h are compared with predicted (subscript *pred*) R_{pred}/h based on the equations included in Table 4 (Fig. 9b). The linear wave tests were predicted with the theoretical equation from Miche (1951) and the empirical equation of Müller (1995) was used for solitary waves, with $L = 2\pi h/(0.75a/h)^{0.5}$ (Lo et al., 2013). The linear wave R_{num}/h are well predicted by Miche (1951) for $\beta = 90°$, while

Table 4
Run-up height R prediction equations of Miche (1951) and Müller (1995).

Reference	R/h	Wave type
Miche (1951)	$\frac{H}{h}\left(\frac{90°}{\beta}\right)^{1/2}$	Linear waves
Müller (1995)	$1.25\left(\frac{a}{h}\right)^{5/4}\left(\frac{a}{L}\right)^{-3/20}\left(\frac{90°}{\beta}\right)^{1/5}$	Solitary waves

deviations of up to 116% are observed for $\beta = 60$ and 75°. These deviations are due to the assumption of complete wave reflection in the theoretical equation. In contrast, the incident waves are only partially reflected from sloped walls (Ursell et al., 1960). The equation of Müller (1995) successfully captures the solitary wave tests, with relatively small deviations.

Fig. 9c, d shows the relative $F_{H,u}/(\rho_w gh^2)$ and $F_H/(\rho_w gh^2)$ versus a/h. $F_{H,u}/(\rho_w gh^2)$ decreases with increasing a/h for all tests and increases with increasing T in the linear wave tests. However, T has a small influence on $F_{H,u}$. The plate stiffness results in negligible deviations of $F_{H,u}/(\rho_w gh^2)$ for the investigated conditions. The larger h_d observed for the flexible plates result in larger forces acting on the downwave side and consequently smaller F_H. As shown in Fig. 9d, this effect is relatively small for most of the tests. In a few tests with $E = 1$ GPa, the plate deformation induced up to 16% larger h_d, with larger p_d acting on the plate, compared to $E = 1000$ GPa. As a result, F_H for $E = 1$ GPa was up to 40% smaller than for $E = 1000$ GPa under these conditions. The data in Fig. 9 will be further discussed and compared with available prediction methods in Section 5.

4.1.4. Numerical plate response

In the offshore tests the natural period of the plate T_s varied from 0.24 to 3.11 s. This was estimated as $1/f_s$ (with f_s from Eq. (9)) with a reduced plate density due to the initial submergence. In the solitary

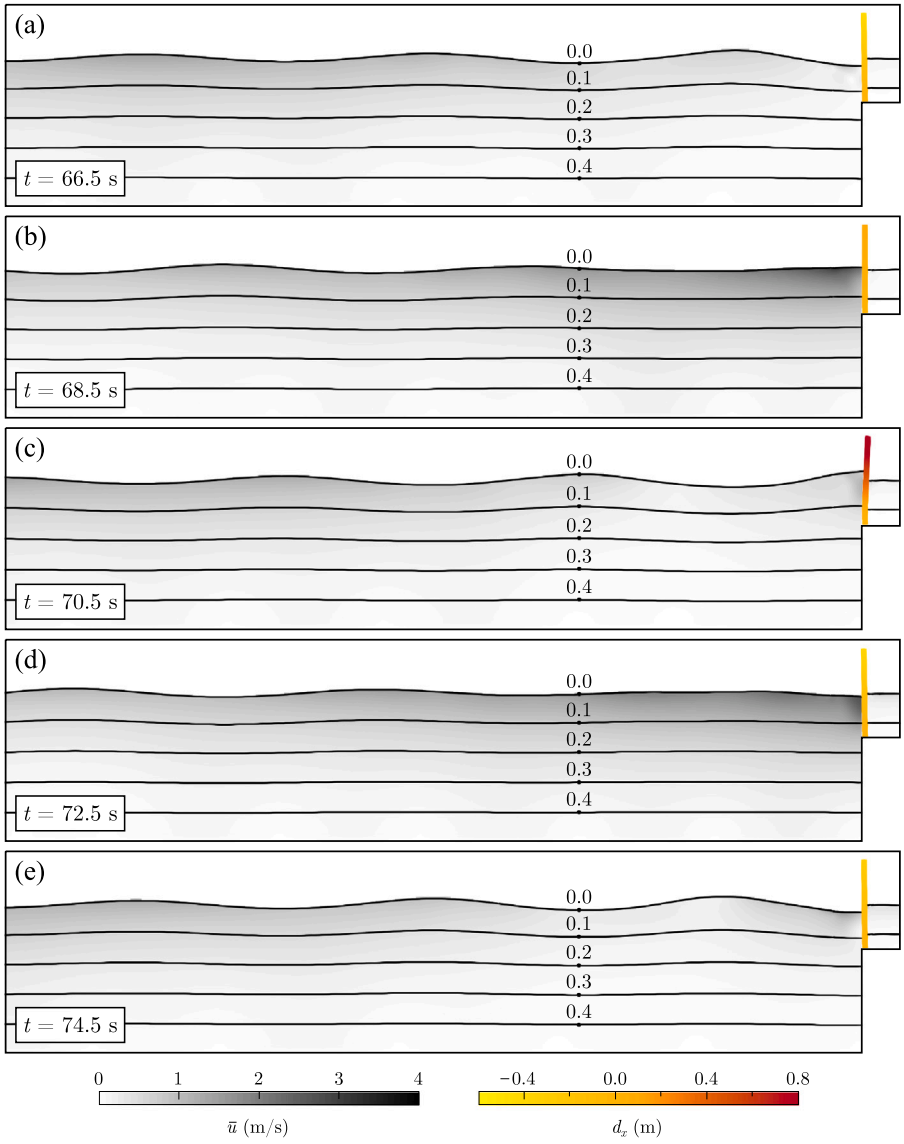

Fig. 7. Snapshot series of a 2D linear wave impacting a plate with $a/h = 0.038$, $T(g/h)^{0.5} = 3.54$, $s = 2.00$ m and $E = 1.00$ GPa showing the mean velocity $\bar{u} = \sqrt{\bar{u}_x^2 + \bar{u}_z^2}$, pressure contours (MPa) and horizontal displacement d_x.

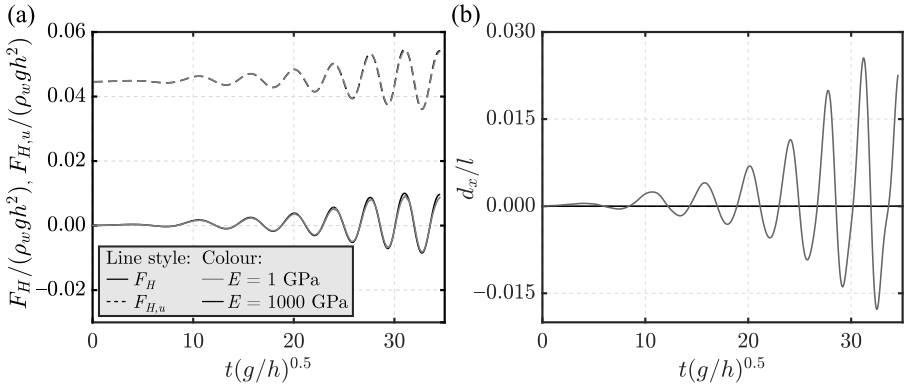

Fig. 8. Offshore tests: time series of the relative (a) total $F_H/(\rho_w g h^2)$ and upstream $F_{H,u}/(\rho_w g h^2)$ forces and (b) horizontal displacement d_x/l at the top end of the offshore plates (Fig. 1a) with $E = 1$ and 1000 GPa and $\beta = 90°$ for a linear wave with $a/h = 0.038$ and $T(g/h)^{0.5} = 3.54$.

wave tests, the wave exerts a quasi static loading on the plate. The ratio T/T_s is relatively large as $T \to \infty$ and the plate does not oscillate over the loading time. On the other hand, the ratio $T/T_s = 1.92$ to 42.16 is relatively small for the linear wave tests. In these tests, the wave impact is of short duration and the plate oscillates with a period close to T (Fig. 8b). No resonance has been observed in the investigated tests.

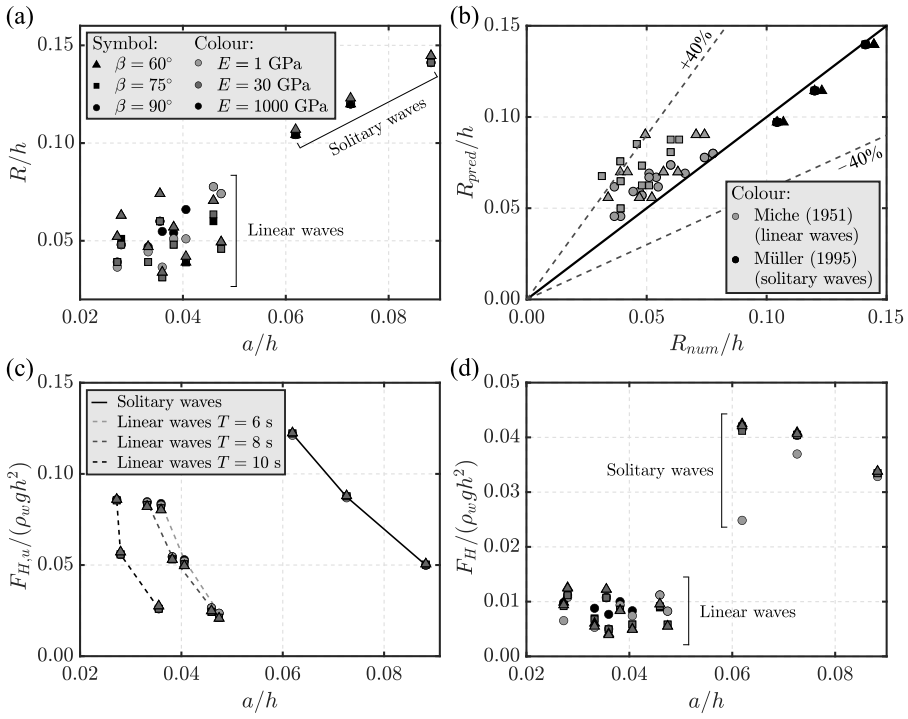

Fig. 9. Offshore tests: (a) relative run-up height R/h versus a/h, (b) predicted R_{pred}/h with (Miche, 1951) for the linear and Müller (1995) for the solitary wave tests (Table 4) versus the numerical R_{num}/h, (c) upwave $F_{H,u}/(\rho_w g h^2)$ and (d) total $F_H/(\rho_w g h^2)$ forces versus a/h for the different plates shown in Table 1.

Fig. 10a shows the maximum $d_{x,max}/l$ versus a/h observed in all offshore tests. The largest $d_{x,max}/l$ were observed in the solitary wave tests and overall $d_{x,max}/l$ decreases for smaller h with constant a. The maximum relative stress component $\sigma_{zz,max}/(\rho_s g l)$ observed along the inner fibre (upwave) versus a/h are shown in Fig. 10b for the solitary wave tests. $\sigma_{zz,max}/(\rho_s g l)$ were observed at or close to the foundation of the plate. The flexible plates show larger $\sigma_{zz,max}/(\rho_s g l)$ compared to the rigid plate.

Based on the Euler-Bernoulli beam theory, d_x and σ_{zz} can be predicted as shown in Appendix B. The maximum predicted $d_{x,max,pred}$ with Eq. (B.11) versus the numerical $d_{x,max,num}$ are shown in Fig. 10c. The coefficient of determination is applied as

$$R^2 = 1 - \frac{\sum_i \left(Y_{num,i} - Y_{pred,i}\right)^2}{\sum_i \left(Y_{num,i} - \bar{Y}\right)^2}, \tag{11}$$

where $Y_{num,i}$ and $Y_{pred,i}$ are the numerical and predicted values and $\bar{Y}$ is the mean of $Y_{num,i}$. The theoretical model tends to overpredict the numerical observations with deviations of up to 149%, whilst in other tests $d_{x,max,num}$ is underestimated by Eq. (B.11).

The observed deviations are partially due to the violation of some of the assumptions for the beam equation. The critical distributed load was assumed static in the beam theory analysis. Conversely, the critical wave pressure distribution is momentarily applied to the plate as a consequence of the dynamic nature of the wave loading. Therefore, the beam theory represents an upper bound estimate of the time varying plate deflections. A further assumption in Appendix B is that the run-up height R corresponds to $2a$. However, this overestimates R_{num} by up to 50%, also contributing to the observed deviations. On the other hand, an estimation of the plate slope $d_{x,max}/l \leq 0.12$ reveals that the small slope assumption is satisfied in all tests. A significantly improved agreement and R^2 values can be achieved by applying an empirical prefactor of 1/2 to $d_{x,max,pred}$, as shown in Fig. 10d.

4.1.5. Numerical 3D tests

Negligible deviations of the main parameters, e.g. p and d_x, have been observed across the plate width in the 3D tests (Section 2.3). Fig. 11a shows the relative upwave $F_{3D,H,u}/(\rho_w g h^3)$ and total $F_{3D,H}/(\rho_w g h^3)$ forces on the 3D rigid and flexible offshore plates. As observed in the 2D simulations (Fig. 8a), the stiffness of the plate results in negligible deviations of $F_{3D,H,u}$, with slight deviations of $F_{3D,H}$ of less than 2%. These are again due to the increase of h_d, and consequently p_d (Fig. 11b), for the flexible plate.

Fig. 11c, d shows the relative displacements d_x/l and stresses $\sigma_{zz}/(\rho_s g l)$ along z/h during the maximum $F_{H,3D}$. As expected, the rigid plate shows negligible d_x/l compared to the flexible plate. The maximum $d_{x,max}/l$ was observed near the centre of the plate at the instant during the maximum $F_{H,3D}$. The maximum $\sigma_{zz,max}/(\rho_s g l)$ were observed at the bottom of the plates, with a deviation between the rigid and flexible plates of 7% only.

4.2. Onshore

4.2.1. Validation of solids4foam with an available laboratory experiment

The numerical model was further validated with a laboratory solitary wave experiment from Kimmoun et al. (2009). The experimental set-up consisted of a flume with a 1:15 sloped shore and a 1.00 m high plate (Fig. 12a). A solitary wave with $a/h = 0.12$ impacting a plastic plate with $s = 5.0$ mm, $E = 3.25$ GPa and $\rho_s = 1190$ kg/m^3 is discussed herein. The plate was fixed at the bottom end and supported at $z = 0.872$ m. The water surface and plate deflections were recorded with 2 cameras. A mesh resolution of $\Delta x = \Delta z = 4.0$ mm was used for the fluid and $\Delta x = 2.5$ mm and $\Delta z = 2.0$ mm for the solid domain. A simulated time of 6 s took approximately 12 days of computation time with 40 CPUs and 500 GB of memory.

The wave overturned in front of the plate and entrapped an air pocket when impacting the plate. This resulted in a complex wave-plate interaction (Peregrine, 2003; Bredmose et al., 2015). Fig. 12b shows the experimental and numerical snapshots at $t = 0.03$ s, where $t = 0.00$ s is the instant when the wave reaches the plate. The water surface elevation is captured well in the simulation, however, the volume of the air pocket is smaller than in the laboratory experiment.

The plate displacements d_x at $z = 0.35$ m are compared in Fig. 12c. The experimental and numerical d_x show similar trends, apart from

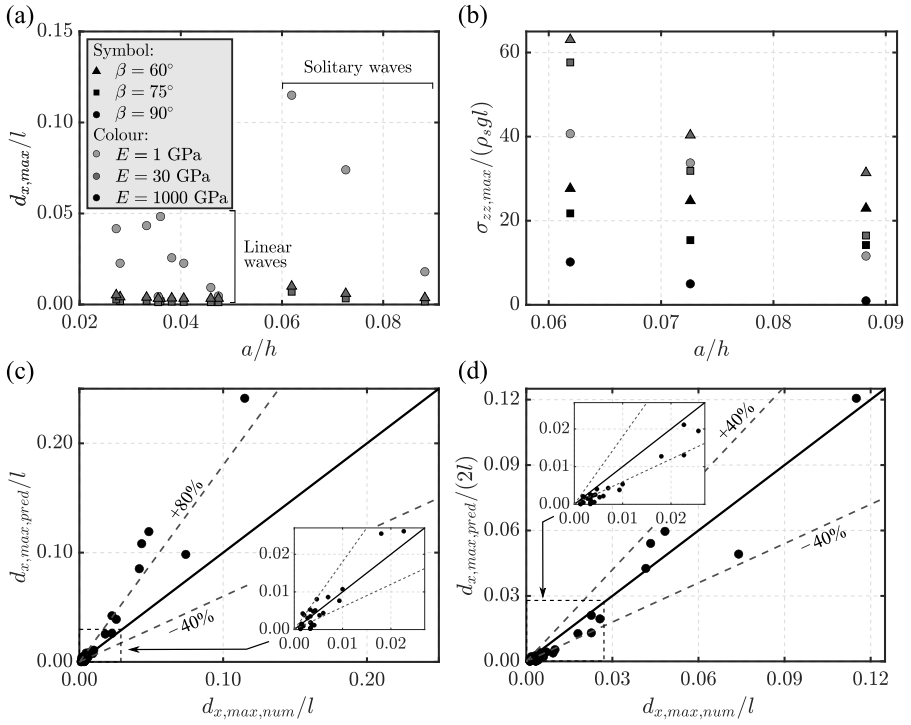

Fig. 10. Plate response for offshore tests: (a) relative maximum displacement $d_{x,max}/l$ versus a/h, (b) relative maximum vertical stress component $\sigma_{zz,max}/(\rho_s g l)$ versus a/h for the solitary wave tests and (c, d) comparison between $d_{x,max,num}/l$ and (c) $d_{x,max,pred}/l$ ($R^2 = -0.42$) and (d) $d_{x,max,pred}/(2l)$ ($R^2 = 0.94$).

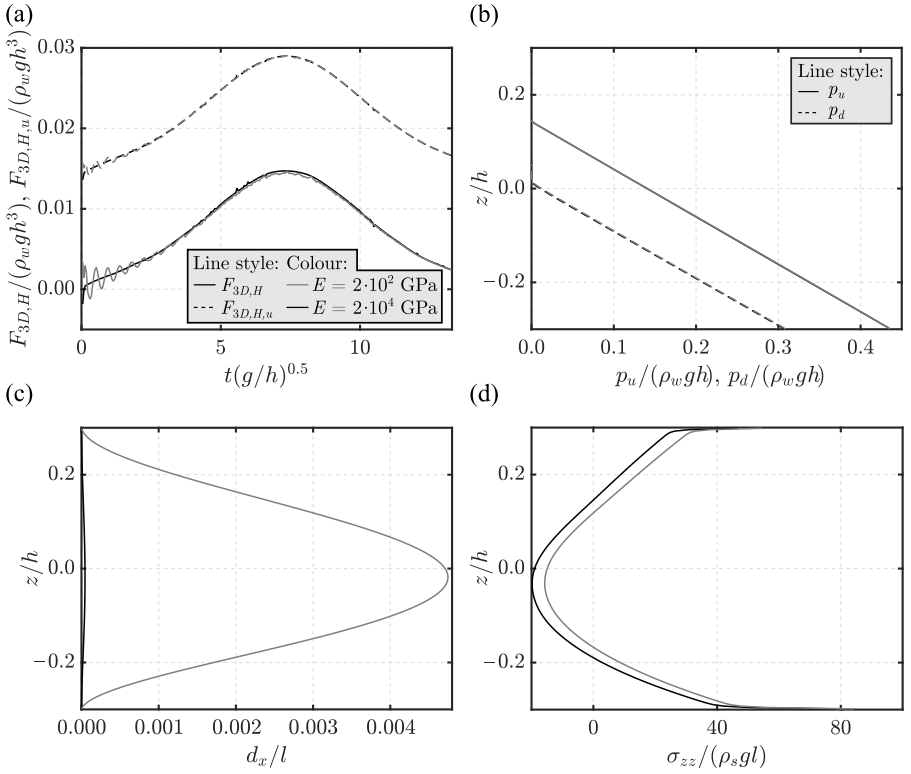

Fig. 11. 3D simulations of offshore tests: (a) relative forces $F_{H,3D}/(\rho_w g h^3)$ and $F_{H,u,3D}/(\rho_w g h^3)$ versus $t(g/h)^{0.5}$, (b) relative pressures $p_u/(\rho_w g h)$ and $p_d/(\rho_w g h)$ along z/h at $y = 7.5$ m, (c) relative displacements d_x/l and (d) relative stresses $\sigma_{zz}/(\rho_s g l)$ at the inner fibre along z/h at $y = 7.5$ m during the maximum force for $E = 2 \cdot 10^2$ and $2 \cdot 10^4$ GPa.

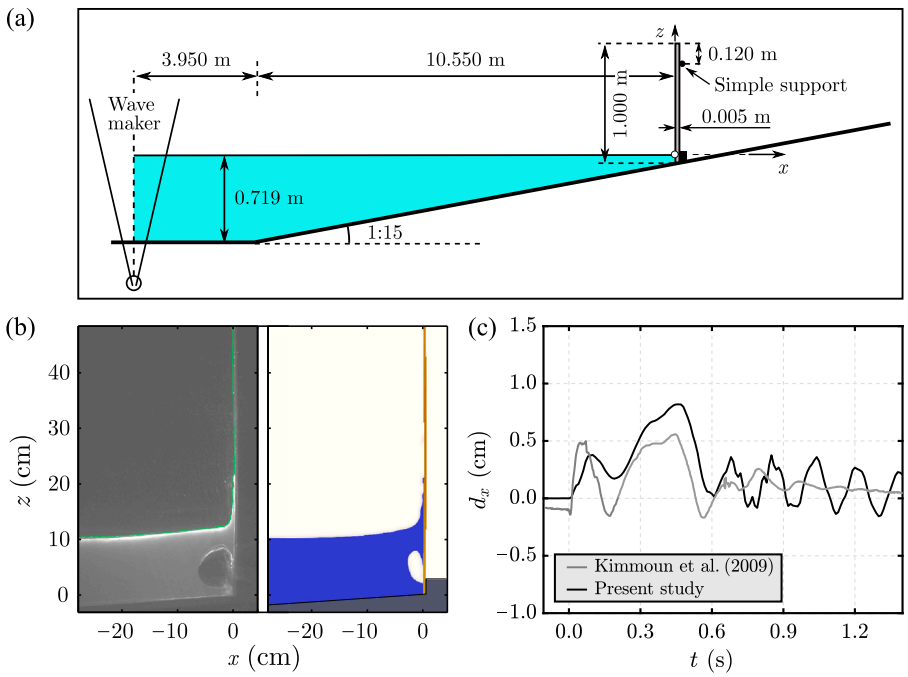

Fig. 12. Validation of solids4foam with an experiment of Kimmoun et al. (2009): (a) experimental set-up, (b) comparison between the laboratory and numerical snapshots at $t = 0.03$ s and (c) horizontal plate displacement d_x at $z = 0.35$ m (after Attili et al., 2022).

some deviations. For $t \leq 0$ s, $d_x < 0$ m was measured in the laboratory experiments, while $d_x = 0$ m is expected. The two peaks of d_x observed in the laboratory experiments at $t \approx 0.08$ and 0.45 s are captured in the simulation, with deviations of up to 35%.

Once the wave was reflected and propagated towards $x \leq 0$ m, the plate oscillated with a certain frequency, as shown in Fig. 12c for $t \geq 0.6$ s. In this phase, the comparison reveals that the laboratory results are affected by a relatively larger damping than the simulation results. In the latter, damping is due to numerical effects only, e.g. temporal discretisation, as physical damping is not modelled in solids4foam. The damping ratio based on the logarithmic decrement of d_x can be evaluated as

$$\zeta = \frac{1}{\sqrt{1 + \left(\frac{2\pi}{\ln \frac{d_{x,i}}{d_{x,i+1}}} \right)^2}} \tag{12}$$

with $d_{x,i}$ and $d_{x,i+1}$ as the displacements of two successive peaks. For 0.6 s $\leq t \leq$ 1.4 s, the averaged ζ resulted in 0.058 and 0.022 for the laboratory and numerical d_x, respectively. The larger ζ and the negative d_x for $t \leq 0$ s shown in the laboratory experiments, in addition to the assumption of incompressible fluid in the simulation, may explain the observed deviations.

4.2.2. A numerical representative test

Fig. 13 shows a snapshot series of an onshore test for a solitary wave with $a/h = 0.4$ impacting the plate TF2 (Table 2). A water column following the wave run-up was observed in front of the plate, which collapses after its kinetic energy is transformed into potential energy (Fig. 13c, d).

4.2.3. Numerical force

The horizontal force F_H acting on the plate shows a first peak F_I at the initial impact followed by a second peak F_{II} (Fig. 14a, b), confirming previous laboratory observations (Linton et al., 2013; Didier et al., 2014). F_{II} is a consequence of the collapse of the water column following the wave run-up at the plate. All tests show a double peak apart from the 5 tests with $a/h = 0.225$ and $z_f/h = 0.000$. In these tests a single peak of F_H was observed, most likely due to the relatively small a/h and large wave length L.

F_{II} is up to 3.3 times larger than F_I, apart from the tests with $a/h = 0.75$ (Fig. 14b). In these tests, due to the relatively large steepness $a/L = 0.09$, surging breaking was observed in proximity of the shore. This resulted in a violent impact on the plate. Fig. 14c, d shows $F_H/(\rho_w g h^2)$ versus a/h and z_f/h. $F_H/(\rho_w g h^2)$ increases with increasing a/h for a constant z_f. For a constant a, $F_H/(\rho_w g h^2)$ decreases with increasing z_f/h, except for the tests with $a/h = 0.75$.

An important finding of this study is that the rigidity of the onshore plate tends to have a negligible effect on F_H (Fig. 14c, d). The largest deviations between the 5 plates under constant wave conditions are observed for large a/h and/or small z/h. Plate R does not necessarily result in the maximum F_H, with deviations of the flexible plates in relation to plate R of up to 3.0% and 17.7% for F_I and F_{II}, respectively. As a result, the design of flexible onshore plates can be based on design approaches for rigid plates combined with a safety factor of 1.2 to account for the observed force variations.

4.2.4. Numerical plate response

The plate deformation depends on the flexural rigidity and the wave loading. The plate R shows negligible horizontal displacements d_x. Maximum deformations were observed for the most flexible plates, namely RS2, TF1 and TF2 (Table 2). Fig. 15a, b shows d_x/l along the centroidal axis and $\sigma_{zz}/(\rho_s g l)$ along the inner fibre of the plate for a representative test with $a/h = 0.4$ at the instant when F_{II} occurred. The plates RS2 showed a maximum $d_{x,max}$ near the centre, while this is observed at the top end for TF1 and TF2. Note that $d_{x,max}$ do not necessarily occur at the instant when the maximum F are observed.

Plate TF2 shows the largest $\sigma_{zz}/(\rho_s g l)$ due to the largest deformation. For all 5 plates, the largest $\sigma_{zz}/(\rho_s g l)$ are observed at the fixing point of the plate. The maximum $d_{x,max}/l$ and $\sigma_{zz,max}/(\rho_s g l)$ are shown as a function of a/h in Fig. 15c, d for plates RS2, TF1 and TF2. Overall, both $d_{x,max}/l$ and $\sigma_{zz,max}/(\rho_s g l)$ increase with increasing a/h for a constant z_f/h. $d_{x,max}/l$ of TF1 are close and/or slightly larger than $d_{x,max}/l$ of RS2. In contrast, $\sigma_{zz,max}/(\rho_s g l)$ of TF1 are smaller than for RS2. Once the wave was reflected, the plate oscillated with a certain

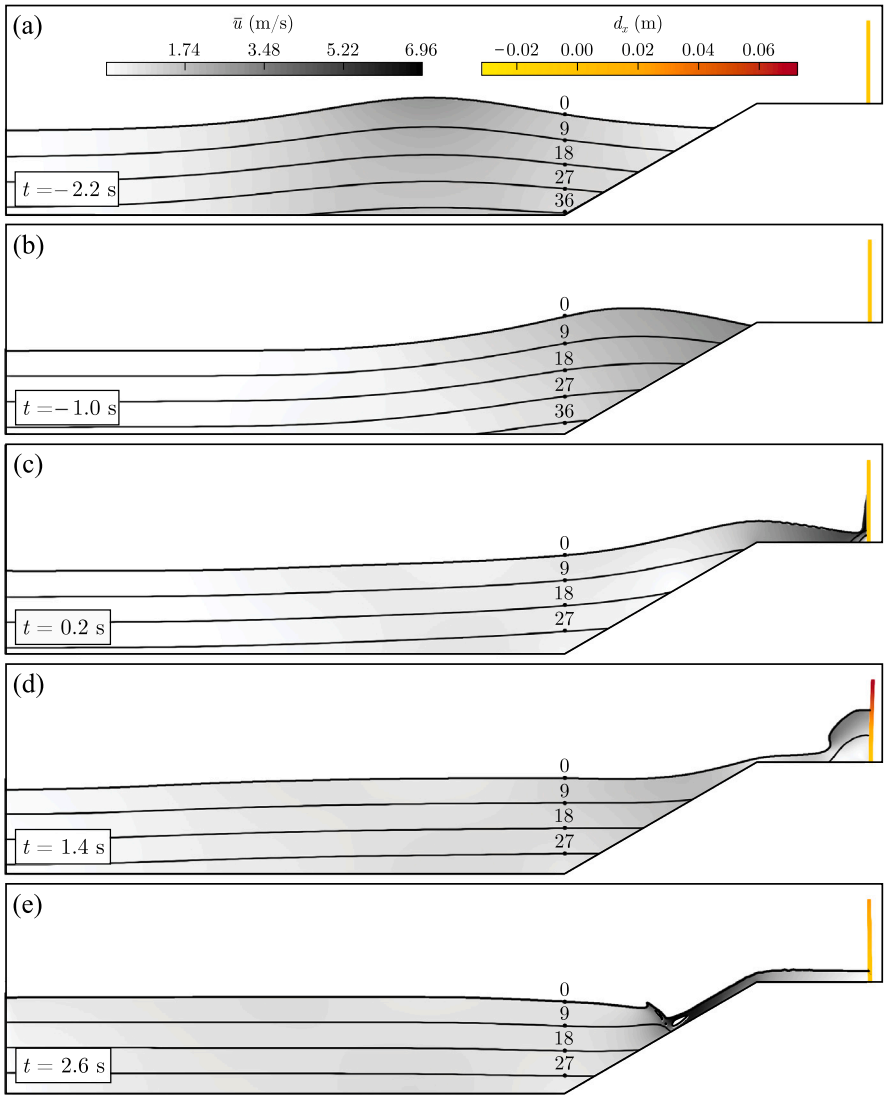

Fig. 13. Snapshot series of a 2D solitary wave impacting an onshore plate with $a/h = 0.40$, $s = 0.15$ m and $E = 1.00$ GPa showing the mean velocity $\bar{u} = \sqrt{\bar{u}_x^2 + \bar{u}_z^2}$, pressure contours (kPa) and horizontal displacement d_x.

frequency f_s. As expected, plates TF1 and TF2 oscillated with f_s close to their natural frequencies (Table 2), namely at $f_s = 4.55$ and 2.27 Hz.

5. Discussion of results

5.1. Offshore

5.1.1. Force

The numerical $F_{H,u,num}/\left(\rho_w g h^2\right)$ in the offshore tests are compared with predictions based on Evers et al. (2019) and Heller et al. (2009). The prediction equation of Evers et al. (2019) has been slightly modified into

$$F_{H,u} = [1 - 1.5(a/h)]^{1/6}(1/2)\rho_w g(2a + h - l_s)^2, \tag{13}$$

to disregard the trapezoidal section of $p(z)$ acting on the substructure at $-h \le z < (-h + l_s)$. The comparison in Fig. 16 reveals that $F_{H,u,num}$ are captured by the prediction method of Evers et al. (2019), operating on the safe side for all tests. The solitary wave tests are predicted well by Eq. (13), with deviations of less than 22% for all investigated stiffnesses. The linear wave tests show the largest underestimations, namely up to 73%. These deviations are likely due to the fact that Eq. (13) relies on more extreme waves, including Stokes 5th order, cnoidal and solitary waves (Attili et al., 2021; Hess et al., 2023).

5.2. Onshore

5.2.1. Transformation into overland flow

Once the waves run-up the shore, they transformed into overland flows before impacting the plates (Fig. 17). The overland flow is characterised by the depth h_s and the depth-averaged velocity $\bar{u}_s$. These are defined at $x = z_f \cot\beta_s + L_s/2$ in the present study. The first force peak F_I (Fig. 14a, b) can be theoretically predicted as a function of h_s and $\bar{u}_s$ with Eq. (1) (taken from Cross, 1967). Fig. 10a shows the predicted $F_{I,pred}/(\rho_w g h^2)$ based on Eq. (1) versus the numerical values $F_{I,num}/(\rho_w g h^2)$ for the tests with plate R. $F_{I,pred}$ was predicted assuming $C_f = 1$ and with the numerical h_s and $\bar{u}_s$ resulting in the maximum $F_{I,pred}$. The comparison shows a good agreement between $F_{I,pred}$ and $F_{I,num}$, however, the predictions of h_s and $\bar{u}_s$ remain challenging. Fuchs and Hager (2015) proposed empirical equations to predict $h_s(x)$ and $\bar{u}_s(x)$, which, however, result in unsatisfactory agreements in the present study with deviations of up to 117%. Further guidelines for the prediction of h_s and $\bar{u}_s$ can be found in design standards (ASCE/SEI 7-16, 2017). In the following section, F_I and F_{II} are directly related to the offshore wave energy E_w such that h_s and $\bar{u}_s$ are no longer required.

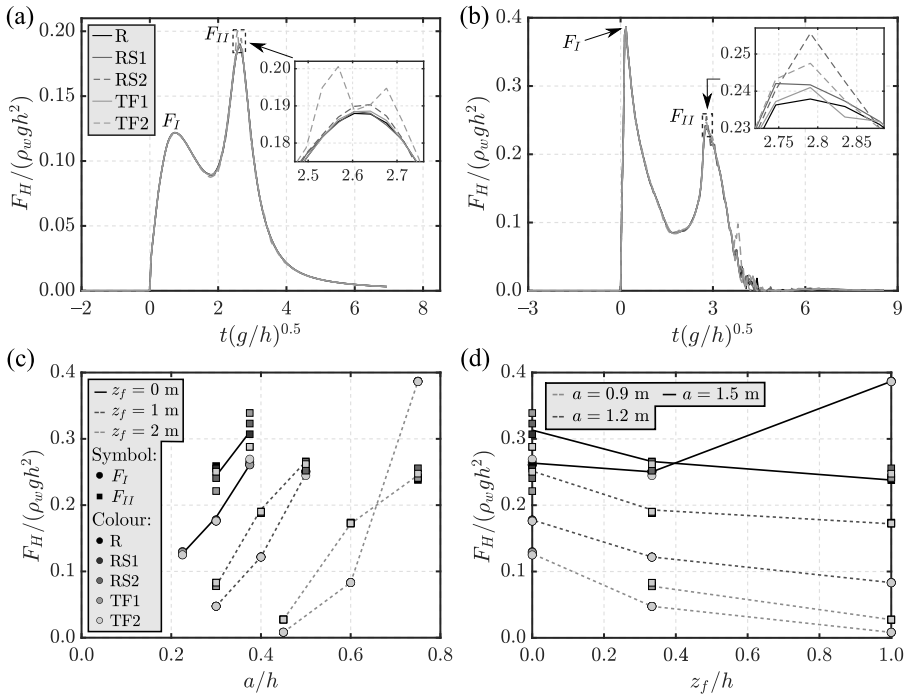

Fig. 14. Plate forces at the 5 plates shown in Table 2 for onshore tests: relative force $F_H/(\rho_w g h^2)$ versus t with (a) $a/h = 0.40$ and (b) $a/h = 0.75$ and (c, d) $F_H/(\rho_w g h^2)$ versus (c) a/h and (d) z_f/h.

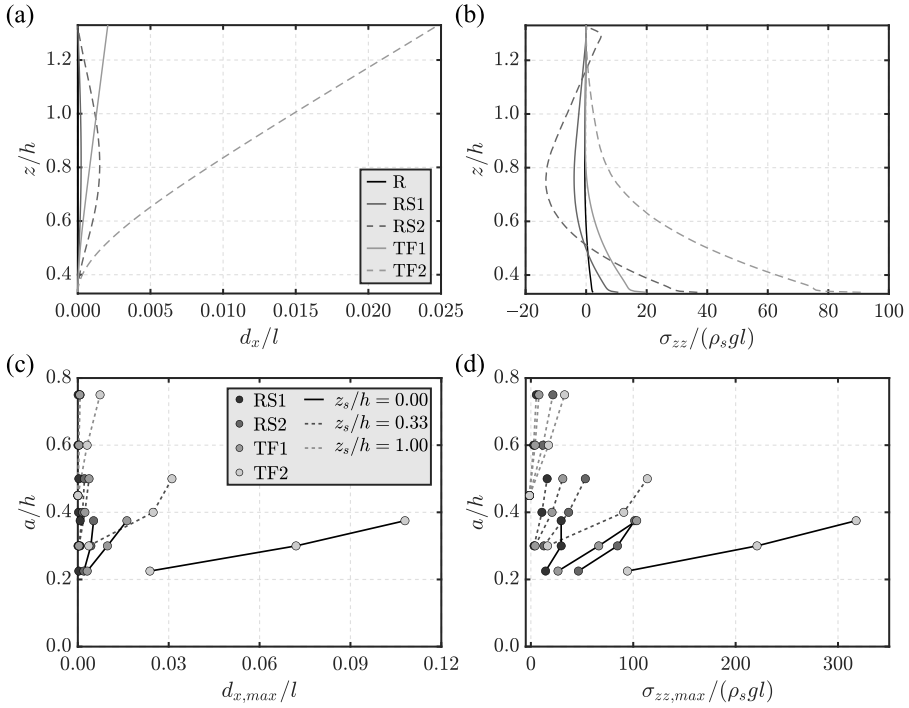

Fig. 15. Plate response for the 5 plates (Table 2) in the onshore tests: (a) dimensionless horizontal displacement d_x/l and (b) vertical stress component $\sigma_{zz}/(\rho_s g l)$ along z/h at $t(g/h)^{0.5} = 2.64$ with $a/h = 0.4$ and maximum (c) $d_{x,max}/l$ and (d) $\sigma_{zz,max}/(\rho_s g l)$ versus a/h.

When a wave propagates and runs-up a slope, its offshore wave energy is transformed into potential and kinetic energies of the overland flow. A portion of the wave energy is consumed during this process by various mechanisms, including bottom friction, reflection from the shore and wave breaking. The energy associated with the reflection from the shore was found to be negligible in the study of Li and Raichlen (2003) and von Häfen et al. (2022) found that the energy dissipated by wave breaking is proportional to a.

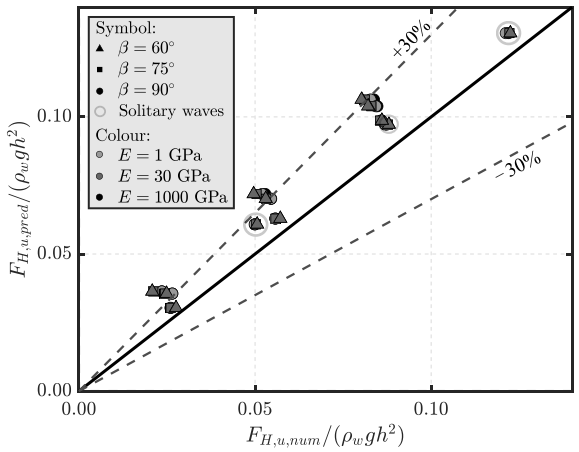

Fig. 16. Comparison of the predicted $F_{H,u,pred}/(\rho_w g h^2)$ (Evers et al., 2019) and numerical $F_{H,u,num}/(\rho_w g h^2)$ for the linear and solitary (encircled) wave tests.

The wave energy per unit width E_w is composed of the kinetic and potential energies. According to Li and Raichlen (2003), E_w of a solitary wave is

$$E_w = \frac{8}{3\sqrt{3}}\rho_w g(ah)^{3/2}. \tag{14}$$

The total energy per unit area of the overland flow E_{of} due to the kinetic and potential components is

$$E_{of} = \frac{1}{2}\rho_w h_s \bar{u}_s^2 + \rho_w g h_s(h + z_f + h_s/2). \tag{15}$$

Based on the energy balance, it can be assumed that E_w is directly proportional to E_{of}. By employing a least-square approach algorithm, the following equation has been derived (Fig. 18b)

$$\frac{E_{of}}{[\rho_w g(h+z_f+a)^2]} = \frac{5}{2}\frac{E_w}{[\rho_w g(h+z_f+a)^3]} - 0.06. \tag{16}$$

The intercept 0.06 in Eq. (16) takes the energy consumed by bottom friction, reflection from the shore and wave breaking into account. The forces F_I and F_{II} observed at the 5 plates (Table 2) were also expressed as a function of E_w as (Fig. 18c, d)

$$\frac{F_I}{[\rho_w g(h+z_f+a)^2]} = \frac{5}{4}\frac{E_w}{[\rho_w g(h+z_f+a)^3]} - 0.04, \tag{17}$$

$$\frac{F_{II}}{[\rho_w g(h+z_f+a+l)^2]} = \frac{2}{3}\frac{E_w}{[\rho_w g(h+z_f+a)^3]} - 0.02. \tag{18}$$

The constants in Eqs. (17) and (18) have been optimised based on a least-square approach algorithm. Eqs. (17) and (18) capture the numerical results well and most of the data deviate less than ±30%. Eq. (17) underestimates the tests with $a/h = 0.75$ by a factor of up to 2.43. Once again, the surging breaking and relatively violent impact on the plate may be the reason for the observed deviations. In this case, advanced turbulence models could provide more accurate results (Larsen and Fuhrman, 2019; Xie and Chu, 2019). Similar correlations are shown in Appendix C to predict $d_{x,max}$ and $\sigma_{zz,max}$.

Eqs. (17) and (18) can be used to predict the maximum surge forces on onshore buildings and infrastructures. To apply these equations, the main dimensionless parameters need to be within the investigated ranges, namely $0.225 \leq a/h \leq 0.750$, $1 \leq L_s/h \leq 2$, $0 \leq z_f/h \leq 1$ and $\beta_s = 30°$. However, Eqs. (17) and (18) may still provide good preliminary estimates when these limitations are moderately violated.

5.2.2. Run-up height

The maximum run-up heights R at the onshore plates are predicted relative to the shore height $(h + z_f)$ as (Fig. 19)

$$\frac{R}{(h+z_f)} = \frac{9}{2}\frac{a}{(h+z_f)} - 0.6. \tag{19}$$

As discussed for Eqs. (17) and (18), a requirement for applying Eq. (19) is that the dimensionless parameters in nature are within the investigated ranges and $\beta_s = 30°$. For solitary wave transformation into overland flow, β_s has an effect on the bottom friction, e.g. smaller β_s result in larger propagation distances, and on the reflection from the shore. For relatively steep slopes, the energy dissipated by bottom friction and reflection from the shore is negligible compared to the energy dissipated by wave breaking (Li and Raichlen, 2003). As a result, a is the most important parameter, such that Eq. (19) provides a reasonable prediction of R even for $\beta_s \neq 30°$. However, for rough slopes and relatively small β_s, the energy dissipation due to bottom friction would have to be taken into account such that Eq. (19) may overestimate R.

6. Conclusions

Waves impacting rigid and flexible plates were investigated based on laboratory and numerical modelling. This study was motivated by the limited knowledge of Wave-Structure Interaction (WSI) effects and the need to further investigate the effect of the plate stiffness on wave forces. The main conclusions are summarised hereafter.

Small-scale laboratory tests of wave impact on offshore plates of different stiffnesses were conducted to validate the numerical model solids4foam. This resulted in a good agreement with the laboratory observations for 2 representative tests, apart from the strain where deviations of up to 59.7% have been observed. The numerical model was further validated with a solitary wave impacting an onshore flexible plate experiment from Kimmoun et al. (2009). A total of 117 numerical tests were conducted to investigate wave impacts on offshore and onshore plates with 2D set-ups. These involved a range of linear and solitary waves with plates of different stiffnesses. The standard k-ϵ model has been used because the turbulence effect was small in the offshore tests and fully turbulent flows were observed in the onshore tests. However, more advanced models, e.g. the Re-Normalised Group k-ϵ and Shear Stress Transport k-ω models, should be employed for more complex processes with strong turbulence and air entrainment (Larsen and Fuhrman, 2019; Xie and Chu, 2019).

The simulations were conducted assuming elastic plates, hence, no energy dissipation due to the material was taken into account. This approximation is suitable for real applications, where energy dissipation is expected to be relatively small.

In the offshore tests, the linear wave run-up heights R were up to 116% overpredicted by the equation of Miche (1951) whilst the solitary wave R were in good agreement with predictions from the equation of Müller (1995) (Fig. 9b). The upstream horizontal forces $F_{H,u}$ were captured by the prediction method based on Evers et al. (2019) for all investigated stiffnesses. The total forces F_H were up to 40% smaller for the tests with Young's moduli $E = 1$ GPa than for tests with $E = 1000$ GPa. These deviations were mostly due to an increase in the downstream water depth h_d as a consequence of the plate deformation. The offshore plate responses were successfully analysed based on the Euler-Bernoulli beam theory (Appendix B). Solitary wave impact on 3D rigid and flexible plates was also simulated. Negligible deviations of the pressures have been observed across the plate width. Once again, the plate stiffness had negligible effects on the wave forces, with relatively small deviations observed in the total force.

The force acting on the onshore plates showed a first F_I and second F_{II} peak, confirming available laboratory observations (Linton et al., 2013; Didier et al., 2014). With the exception of a few tests where surging breaking was observed, F_{II} was up to 3.3 times larger than F_I. The rigidity of the plate had a negligible effect on the wave force in most of the tests (Fig. 14c, d). For constant wave conditions, the largest deviations between the 5 plates (Table 2) were observed for large wave amplitude relative to the water depth a/h and/or small relative shore freeboard z_f/h. The rigid plate did not necessarily result in the maximum wave forces, with deviations of the flexible plates

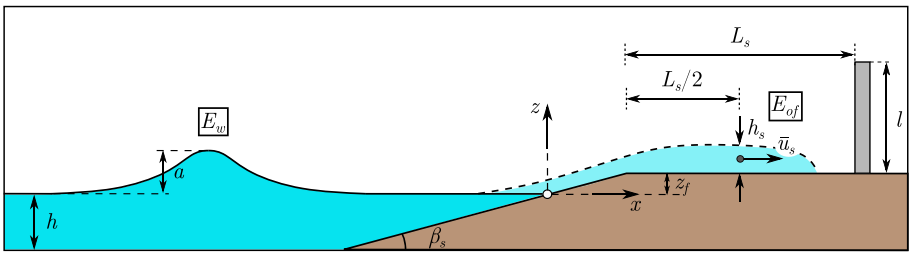

Fig. 17. Sketch with the main parameters of a solitary wave and its transformation to overland flow.

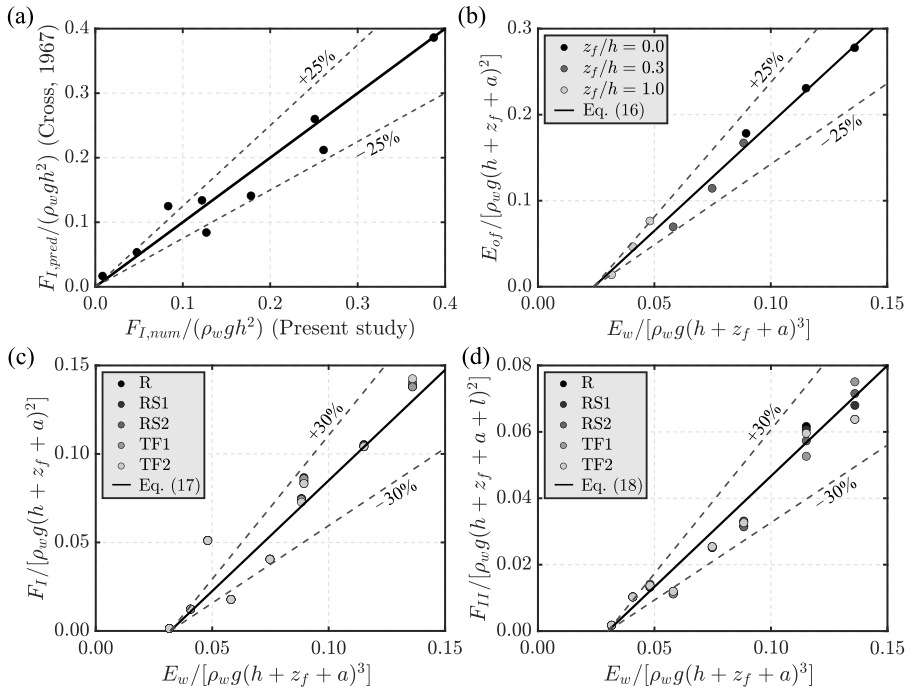

Fig. 18. Overland flow: (a) comparison of the predicted (Cross, 1967) and numerical $F_I/(\rho_w g h^2)$ ($R^2 = 0.93$) at plate R, (b) energy of the overland flow $E_{of}/[\rho_w g(h+z_f+a)^2]$ with Eq. (16) ($R^2 = 0.98$) for plate R, (c) $F_I/[\rho_w g(h+z_f+a)^2]$ with Eq. (17) ($R^2 = 0.90$) versus the wave energy $E_w/[\rho_w g(h+z_f+a)^3]$ and (d) $F_{II}/[\rho_w g(h+z_f+a+l)^2]$ versus $E_w/[\rho_w g(h+z_f+a)^3]$ with Eq. (18) ($R^2 = 0.96$) for all 5 plates in Table 2.

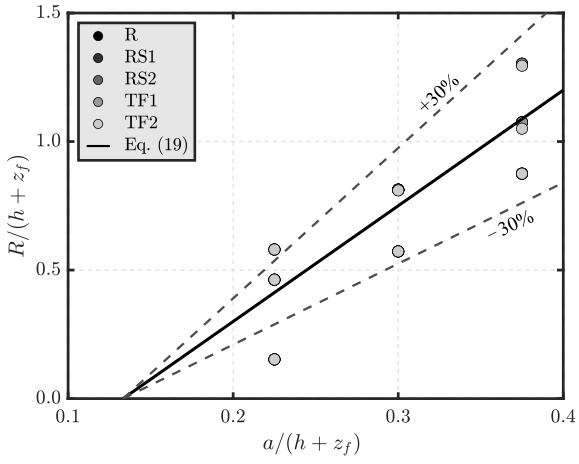

Fig. 19. Dimensionless run-up $R/(h+z_f)$ versus the dimensionless wave amplitude $a/(h+z_f)$ with Eq. (19) ($R^2 = 0.75$).

in relation to the rigid one of up to 3.0 and 17.7% for F_I and F_{II}, respectively.

The solitary wave transformation into overland flow was also analysed for the onshore tests. New semi-theoretical correlations based on the solitary wave energy were derived. These provide the wave forces for both F_I and F_{II} and plate responses, including the horizontal displacement and vertical stresses. In addition, the maximum R were approximated in function of a, h and z_f.

To sum up, the flexible plates did not necessarily result in smaller wave forces compared to the rigid ones for the investigated conditions. In the offshore tests, the plate stiffness had a negligible effect on the upwave forces. However, smaller total forces were observed for more deformable offshore plates. Based on that, the actual stiffness of the plate needs to be taken into account for the design of offshore plates. The total forces on the onshore plates were unaffected by the plate stiffness in most tests. Up to 17% deviations were observed in a few tests, however with the rigid plate not always resulting in the largest force. Therefore, the design of both rigid and flexible onshore plates can be based on design approaches for rigid plates combined with a safety factor of 1.2 to account for the observed force variations within this study.

Ongoing and future work will focus on the scaling and scale effects in WSI phenomena. This, along with the findings of Attili et al. (2021)

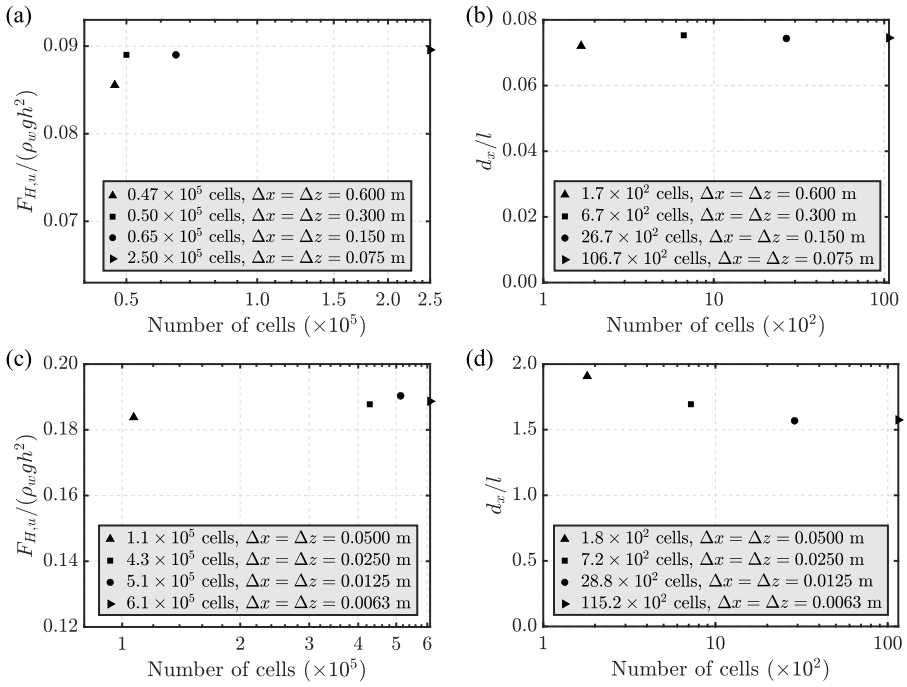

Fig. A.1. Convergence tests: semi-logarithmic diagramme for the relative (a, c) force $F_{H,u}/(\rho_w g h^2)$ and (b, d) horizontal displacement d_x/l with the number of cells and mesh size $\Delta x = \Delta z$ for an (a, b) offshore and (c, d) onshore test.

and of the present article, are aimed at enhancing the physical understanding and modelling as well as support the design of coastal and offshore structures.

CRediT authorship contribution statement

Tommaso Attili: Formal analysis, Investigation, Methodology, Validation, Visualization, Writing – original draft, Writing – review & editing. **Valentin Heller:** Conceptualization, Funding acquisition, Methodology, Project administration, Supervision, Validation, Writing – review & editing. **Savvas Triantafyllou:** Conceptualization, Methodology, Supervision, Validation, Writing – review & editing.

Declaration of competing interest

The authors declare that they have no known competing financial interests or personal relationships that could have appeared to influence the work reported in this paper.

Data availability

Data will be made available on request.

Acknowledgements

The authors would like to thank Dr. Ricardo Correia and Dr. Sándor Erdődy from the Optics and Photonics Group for providing the fibre optic sensors used in the laboratory tests. Dr. Walid Tizani from the Centre for Structural Engineering & Informatics is acknowledged for lending the interrogator. Mr. Sam Cook and Mr. Alistair Palmer are acknowledged for supporting the experimental design and for helping with the measurement equipment for the laboratory experiments. The PhD study of Tommaso Attili is financially supported by the University of Nottingham Vice-Chancellor's Scholarship for Research Excellence. The third author acknowledges the support of the European Union's Horizon research and innovation programme under the Marie Sklodowska-Curie Individual Fellowship grant "AI2AM: Artificial Intelligence driven topology optimisation of Additively Manufactured Composite Components", No. 101021629. The simulations were conducted on the HPC cluster Augusta at the University of Nottingham.

Appendix A. Convergence tests

Convergence tests were conducted for both the offshore and onshore set-ups (Fig. 1). Resolutions of $\Delta x = \Delta z = 0.075$, 0.150, 0.300 and 0.600 m were investigated in the offshore case. The finest resolutions $\Delta x = \Delta z = 0.075$, 0.150 and 0.300 m were used in a 25 m × 32 m refined area only (Fig. 1a), with larger meshes $\Delta x = \Delta z = 0.300$ and 0.600 m in the remainder of the domain.

Convergence tests were conducted with a solitary wave with $a/h = 0.073$ and $L = 2\pi h/(0.75a/h)^{0.5} = 1346$ m (Lo et al., 2013) impacting a plate with $E = 1$ GPa. $F_{H,u}/(\rho_w g h^2)$ and d_x/l are shown versus the number of cells and mesh sizes in Fig. A.1a, b. $\Delta x = \Delta z = 0.150$ m was used for the main tests as convergence is achieved. This resulted in negligible differences (<1%) with $\Delta x = \Delta z = 0.075$ m, for both $F_{H,u}$ and d_x, requiring approximately 1/4 of the computational time.

A solitary wave with $a/h = 0.4$ and $L = 2\pi h/(0.75a/h)^{0.5} = 34.4$ m (Lo et al., 2013) impacting plate RS2 (Table 2) has been simulated to investigate the optimal mesh resolution for the onshore tests. Resolutions of $\Delta x = \Delta z = 0.0063$, 0.0125, 0.0250 and 0.0500 m were investigated. The finest resolutions $\Delta x = \Delta z = 0.0063$ and 0.0125 m were used in a 1.40 m × 3.00 m area surrounding the plate, while $\Delta x = \Delta z = 0.0250$ m was used in the rest of the domain (Fig. 1b). $F_{H,u}/(\rho g h^2)$ overall decreases with rougher resolutions, while d_x/l increases (Fig. A.1c, d). $\Delta x = \Delta z = 0.0125$ m resulted in the optimal mesh resolution. This shows deviations of only 0.9% and 0.4% for $F_{H,u}/(\rho_w g h^2)$ and d_x/l, respectively, in relation to $\Delta x = \Delta z = 0.0063$ m and required 1/2 of the computational time.

Appendix B. An application of the Euler-Bernoulli beam theory for offshore plates

The Euler-Bernoulli beam theory describes the behaviour of beams under axial forces and bending (Timoshenko, 1983). By assuming that plane beam sections remain plane and perpendicular to the deformed neutral axis and the slope $\mathrm{d}d_x$ / $\mathrm{d}z$ is small, the beam deflection results in

$$E I \frac{\mathrm{d}^4 d_x}{\mathrm{d}z^4} = p(z). \tag{B.1}$$

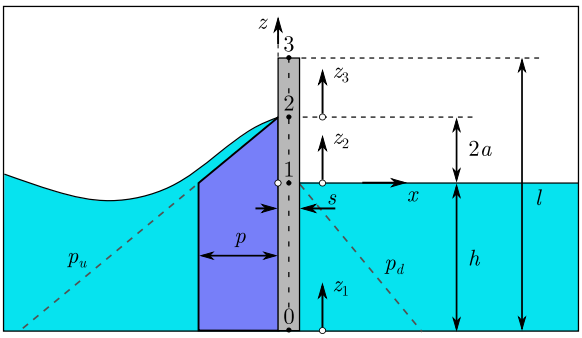

Fig. B.1. Sketch with the main parameters and pressure distribution of a wave impact on offshore plates.

Table B.1
Boundary conditions at the 4 significant points for the offshore plate of Fig. B.1.

Point 0	Point 1	Point 2	Point 3
$d_x(z_1=0)=0$	$d_x(z_1=h)=d_x(z_2=0)$	$d_x(z_2=2a)=d_x(z_3=0)$	–
$\left.\frac{\mathrm{d}d_x}{\mathrm{d}z_1}\right\|_{z_1=0}=0$	$\left.\frac{\mathrm{d}d_x}{\mathrm{d}z_1}\right\|_{z_1=h}=\left.\frac{\mathrm{d}d_x}{\mathrm{d}z_2}\right\|_{z_2=0}$	$\left.\frac{\mathrm{d}d_x}{\mathrm{d}z_2}\right\|_{z_2=2a}=\left.\frac{\mathrm{d}d_x}{\mathrm{d}z_3}\right\|_{z_3=0}$	–
–	$M(z_1=h)=M(z_2=0)$	$M(z_2=2a)=M(z_3=0)$	$M(z_3=l-h-2a)=0$
–	$Q(z_1=h)=Q(z_2=0)$	$Q(z_2=2a)=Q(z_3=0)$	$Q(z_3=l-h-2a)=0$

In Eq. (B.1), $I=bs^3/12$ is the moment of inertia of the beam cross-section, with b as the beam width, and $p(z)$ represents a distributed static load. The moment curvature relation is

$$M=-EI\frac{\mathrm{d}^2d_x}{\mathrm{d}z^2} \tag{B.2}$$

and the shear force is evaluated as

$$Q=-EI\frac{\mathrm{d}^3d_x}{\mathrm{d}z^3}. \tag{B.3}$$

In the present study the bending moment in the beam is defined positive when it produces a compressive stress at the downwave face of the beam.

Based on the numerical observations, the offshore plate response may be assumed quasi-static as it is in phase with the excitation and no transient oscillations emerge. Under these assumptions, Eq. (B.1) can be applied to the offshore plates where $b=1$ m and $p(z)$ due to hydrostatic and wave pressures is approximated as shown in Fig. B.1, with $p=\rho_w g 2a[1-1.5(a/h)]^{1/6}$ (Heller et al., 2009; Evers et al., 2019). By integrating Eq. (B.1) between points 0-1, 1-2 and 2-3 (Fig. B.1) the following 3 equations were obtained

$$EId_x(z_1)=p\frac{z_1^4}{24}+C_1\frac{z_1^3}{6}+C_2\frac{z_1^2}{2}+C_3z_1+C_4,\quad \text{for } 0\le z_1<h, \tag{B.4}$$

$$EId_x(z_2)=p\left(1-\frac{z_2}{10a}\right)\frac{z_2^4}{24}+C_5\frac{z_2^3}{6}+C_6\frac{z_2^2}{2}+C_7z_2+C_8,\quad \text{for } 0\le z_2<2a \text{ and} \tag{B.5}$$

$$EId_x(z_3)=C_9\frac{z_3^3}{6}+C_{10}\frac{z_3^2}{2}+C_{11}z_3+C_{12},\quad \text{for } 0\le z_3\le(l-h-2a). \tag{B.6}$$

For the sake of conciseness, the substructure has been omitted herein and $\beta=90°$ has been used. In the presence of a substructure (Fig. 1a), Eqs. (B.4) and (B.6) are valid for $0\le z_1<(h-l_s)$ and $0\le z_3<(l-h+l_s-2a)$, respectively. For $\beta<90°$, Eqs. (B.4) to (B.6) rely on the x- and z-axis rotated clockwise by $(90°-\beta)$ compared to $\beta=90°$.

Table B.2
Values for the constants in Eqs. (B.4), (B.5) and (B.6).

Constant	Value
C_1	$-ph-pa$
C_2	$p\frac{h^2}{2}+pha+\frac{p}{6}(2a)^2$
C_3	0
C_4	0
C_5	$-pa$
C_6	$\frac{p}{6}(2a)^2$
C_7	$p\frac{h^3}{6}+p\frac{h^2}{2}a+p\frac{h}{6}(2a)^2$
C_8	$p\frac{h^4}{8}+p\frac{h^3}{3}a+p\frac{h^2}{12}(2a)^2$
C_9	0
C_{10}	0
C_{11}	$p\frac{h^3}{6}+p\frac{h^2}{2}a+p\frac{h}{6}(2a)^2+\frac{p}{24}(2a)^3$
C_{12}	$p\frac{h^4}{8}+p\frac{h^3}{3}2a+p\frac{h^2}{3}(2a)^2+p\frac{h}{6}(2a)^3+\frac{p}{30}(2a)^4$

A number of boundary conditions can be imposed at points 0, 1, 2 and 3 (Table B.1). These include zero displacement and rotation at point 0, continuity of the displacement, rotation, moment and shear force at points 1 and 2 and zero moment and shear force at point 3. These boundary conditions result in a system of 12 linear equations with C_i, for $i=1,\ldots,12$ unknowns, with the solution shown in Table B.2.

The Euler-Bernoulli beam equation can also be used to describe the distribution of the vertical stresses at the inner fibre of the beam

$$\sigma_{zz}(z)=\frac{s}{2}E\frac{\mathrm{d}^2d_x}{\mathrm{d}z^2}. \tag{B.7}$$

By combining Eq. (B.7) with the second derivatives of Eqs. (B.4) to (B.6)

$$\sigma_{zz}(z)=\frac{s}{2I}\left(p\frac{z_{s1}^2}{2}+C_1z_{s1}+C_2\right),\ \text{for } 0\le z_{s1}<h, \tag{B.8}$$

$$\sigma_{zz}(z)=\frac{s}{2I}\left[p\left(1-\frac{z_{s2}}{6a}\right)\frac{z_{s2}^2}{2}+C_5z_{s2}+C_6\right],\ \text{for } 0\le z_{s2}\le 2a \text{ and} \tag{B.9}$$

$$\sigma_{zz}(z)=0,\ \text{for } z_3>0. \tag{B.10}$$

The comparisons between the numerical and predicted d_x/l and $\sigma_{zz}/(\rho_s gl)$ based on Eqs. (B.4) to (B.6) and Eqs. (B.8) to (B.10), respectively, with the constants in Table B.2, are shown in Fig. B.2 for

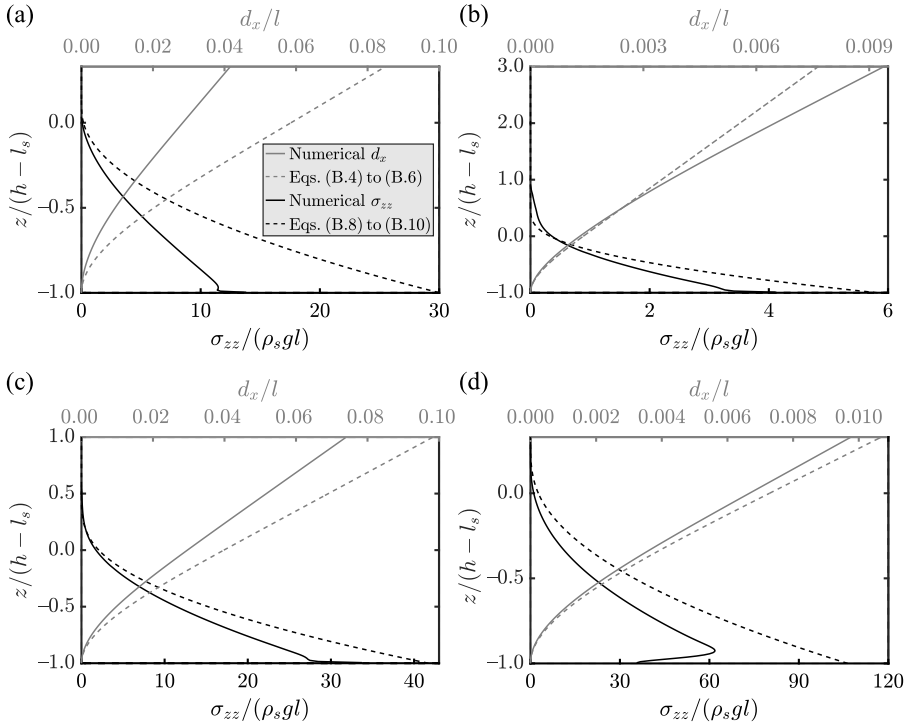

Fig. B.2. Comparison of the predicted and numerical (a) d_x/l ($nRMSE = 0.27$) and $\sigma_{zz}/(\rho_s g l)$ ($nRMSE = 0.22$) for a linear wave test with $a/h = 0.027$, $T(g/h)^{0.5} = 4.13$, $E = 1$ GPa and $\beta = 90°$, (b) d_x/l ($nRMSE = 0.10$) and $\sigma_{zz}/(\rho_s g l)$ ($nRMSE = 0.09$) for a linear wave test with $a/h = 0.046$, $T(g/h)^{0.5} = 3.84$, $E = 1$ GPa and $\beta = 90°$, (c) d_x/l ($nRMSE = 0.14$) and $\sigma_{zz}/(\rho_s g l)$ ($nRMSE = 0.10$) for a solitary wave test with $a/h = 0.073$, $E = 1$ GPa and $\beta = 90°$ and (d) d_x/l ($nRMSE = 0.04$) and $\sigma_{zz}/(\rho_s g l)$ ($nRMSE = 0.17$) for a solitary wave test with $a/h = 0.062$, $E = 30$ GPa and $\beta = 60°$.

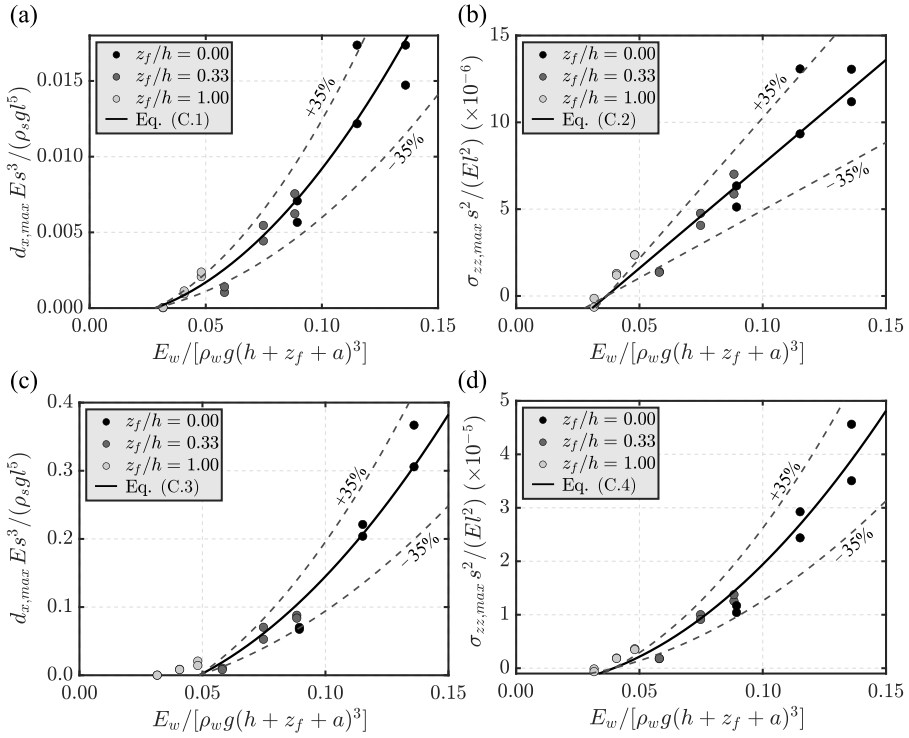

Fig. C.1. Plate response in the onshore tests: maximum relative (a) displacement $d_{x,max} Es^3/(\rho_s g l^5)$ with Eq. (C.1) ($R^2 = 0.93$) and (b) stress $\sigma_{zz,max} s^2/(El^2)$ with Eq. (C.2) ($R^2 = 0.93$) for plates RS and (c) $d_{x,max} Es^3/(\rho_s g l^5)$ with Eq. (C.3) ($R^2 = 0.95$) and (d) $\sigma_{zz,max} s^2/(El^2)$ with Eq. (C.4) ($R^2 = 0.96$) for plates TF versus the dimensionless wave energy $E_w/[\rho_w g(h + z_f + a)^3]$.

4 representative tests. The maximum $d_{x,max}$ at the plate top end results from Eq. (B.6) with $z_{s3} = l - h + l_s - 2a$ in

$$d_{x,max} = 12\frac{C_{11}(l - h + l_s - 2a) + C_{12}}{Es^3}. \tag{B.11}$$

While such an application of the static Euler-Bernoulli beam theory provides a reasonable prediction of the offshore plate responses, future studies should include time varying load distributions for more complex wave-plate interactions.

Appendix C. Correlations of the onshore plate response

The maximum $d_{x,max}$ and $\sigma_{zz,max}$ are expressed as a function of the offshore wave energy E_w for the onshore tests. For the roller support plates the following equations have been derived (Fig. C.1a, b)

$$\frac{d_{x,max}Es^3}{\rho_s g l^5} = \left(\frac{E_w}{[\rho_w g(h + z_f + a)^3]}\right)^2 - 8.0 \cdot 10^{-4}, \tag{C.1}$$

$$\frac{\sigma_{zz,max}s^2}{El^2} = 1.2 \cdot 10^{-4}\left(\frac{E_w}{[\rho_w g(h + z_f + a)^3]}\right) - 4.4 \cdot 10^{-6}. \tag{C.2}$$

For the top free plates, $d_{x,max}$ and $\sigma_{zz,max}$ are expressed as (Fig. C.1c, d)

$$\frac{d_{x,max}Es^3}{\rho_s g l^5} = 19.0\left(\frac{E_w}{[\rho_w g(h + z_f + a)^3]}\right)^2 - 0.04, \tag{C.3}$$

$$\frac{\sigma_{zz,max}s^2}{El^2} = 2.3 \cdot 10^{-3}\left(\frac{E_w}{[\rho_w g(h + z_f + a)^3]}\right)^2 - 3.6 \cdot 10^{-6}. \tag{C.4}$$

Notation

a	Wave amplitude, m
b	Beam width, m
C	Courant number
C_f	Force coefficient in Cross (1967)
$C_{1,2,\ldots 12}$	Constants of the offshore plate displacement, $Nm^{0,1,2\text{ or }3}$
$\mathbf{D}_F$	Deformation gradient
$\mathbf{d}$	Displacement vector, m
d_x	Plate displacement component along x-axis, m
E	Young's modulus, N/m^2
E_{of}	Overland flow energy per unit area, J/m^2
E_w	Offshore wave energy per unit width, J/m
F	Force on plate per unit width resulting from a wave and hydrostatic pressure, N/m
F_I	First force peak on plate per unit width resulting from a surge, N/m
F_{II}	Second force peak on plate per unit width resulting from a surge, N/m
F_{3D}	Force on plate resulting from a wave and hydrostatic pressure, N
f_s	Natural frequency of a plate, Hz
f_σ	Surface tension force per unit volume, N/m^3
$\mathbf{g}$	Gravitational acceleration vector, m/s^2
g	Gravitational acceleration, m/s^2
H	Wave height, m
h	Water depth, m
I	Identity matrix
I	Moment of inertia, m^4
i	Index for the i-th data value
J	Determinant of $\mathbf{D}_F$
k	Turbulent kinetic energy, m^2/s^2
L	Wave length, m
L_s	Shore length, m
l	Plate height, m
l_s	Substructure height, m
M	Bending moment, N m
N	Number of the considered pressure values
$nRMSE$	Normalised Root Mean Square Error
p	Pressure, N/m^2
$\bar{p}$	Mean pressure, N/m^2
Q	Shear force, N
R	Wave run-up height, m
R^2	Coefficient of determination
s	Plate thickness, m
T	Wave period, s
T_s	Natural period of the plate, s
t	Time, s
$\bar{\mathbf{u}}$	Mean fluid velocity vector, m/s
$\overline{\mathbf{u}'\mathbf{u}'}$	Turbulent stress tensor, N/m^2
$\bar{u}$	Depth-averaged velocity, m/s
$\mathbf{u}_r$	Compression velocity vector, m/s
$\bar{u}_x, \bar{u}_y, \bar{u}_z$	Mean fluid velocity component along x-, y- and z-axis, m/s
x, y, z	x-, y- and z-axis, m
Y	Observed values
$\bar{Y}$	Mean of numerical values
z_f	Shore freeboard, m
α	Fraction of volume
β	Plate inclination, °
Δt	Time step, s
$\Delta x, \Delta y, \Delta z$	Cell sizes, m
ε	Turbulence energy dissipation rate, m^2/s^3
ε_{zz}	Strain component of the plate along z-axis
ζ	Damping ratio
η	Water surface elevation, m
μ	Fluid dynamic viscosity, Ns/m^2
π	Mathematical constant
ρ	Density, kg/m^3
$\boldsymbol{\sigma}_s$	Stress tensor, N/m^2
σ_{zz}	Normal plate stress component along z-axis, N/m^2
ω	Turbulence energy dissipation rate, m^2/s^3

Subscripts

a	Air
d	Downwave
exp	Experimental
H	Horizontal
max	Maximum
min	Minimum
num	Numerical
$pred$	Predicted
s	Shore, solid
u	Upwave
w	Water

Abbreviations

CFD	Computational Fluid Dynamics
CFL	Courant-Friedrichs-Lewy
CPU	Central Processing Unit
CSD	Computational Structural Dynamics
FE 4.0	Foam-Extend 4.0
FEM	Finite Element Method

FPSO	Floating Production Storage and Offloading
FVM	Finite Volume Method
HPC	High Performance Computing
LC	Load Cell
MPS	Moving Particle Semi-implicit
OF	OpenFOAM
PIMPLE	Combination of Pressure Implicit Splitting Operator (PISO) and Semi-Implicit Method for Pressure-Linked Equations (SIMPLE)
PPT	Precision Pressure Transducer
R	Rigid Plate
RANS	Reynolds-Averaged Navier-Stokes
RS	Roller Support
SG	Strain Gauge
SPH	Smoothed Particle Hydrodynamics
TF	Top Free
VOF	Volume Of Fluid
WEC	Wave Energy Converter
WG	Wave Gauge
WSI	Wave-Structure Interaction
2D	Two-dimensional (flume)
3D	Three-dimensional (basin)

References

Aguerre, H.J., Damián, S.M., Gimenez, J.M., Nigro, N.M., 2013. Modeling of compressible fluid problems with OpenFOAM using dynamic mesh technology. Mec. Comput. 32 (13), 995–1011.

Antoci, C., Gallati, M., Sibilla, S., 2007. Numerical simulation of fluid-structure interaction by SPH. Comput. Struct. 85 (11), 879–890.

ASCE/SEI 7-16, 2017. Minimum Design Loads and Associated Criteria for Buildings and Other Structures. American Society of Civil Engineers, Standards.

Attili, T., Heller, V., Triantafyllou, S., 2021. A numerical investigation of tsunamis impacting dams. Coast. Eng. 169, 103942.

Attili, T., Heller, V., Triantafyllou, S., 2022. Numerical investigation of waves interacting with rigid and flexible plates. In: 39th International Association for Hydro-Environmental Engineering and Research World Congress. pp. 4438–4447.

Brackbill, J.U., Kothe, D.B., Zemach, C., 1992. A continuum method for modeling surface tension. J. Comput. Phys. 100 (2), 335–354.

Bredmose, H., Bullock, G.N., Hogg, A.J., 2015. Violent breaking wave impacts. Part 3. Effects of scale and aeration. J. Fluid Mech. 765, 82–113.

Cardiff, P., Karač, A., Jaeger, P.D., Jasak, H., Nagy, J., Ivanković, A., Tuković, Z., 2018. An open-source finite volume toolbox for solid mechanics and fluid-solid interaction simulations. ArXiv Prepr ArXiv180810736.

Chaplin, J.R., Heller, V., Farley, F.J.M., Hearn, G.E., Rainey, R.C.T., 2012. Laboratory testing the Anaconda. Phil. Trans. R. Soc. A 370, 403–424.

Chen, F., Heller, V., Briganti, R., 2020. Numerical modelling of tsunamis generated by iceberg calving validated with large-scale laboratory experiments. Adv. Water Resour. 142, 103647.

Chen, L., Stagonas, D., Santo, H., Buldakov, E., Simons, R., Taylor, P., Zang, J., 2019. Numerical modelling of interactions of waves and sheared currents with a surface piercing vertical cylinder. Coast. Eng. 145, 65–83.

Chen, L., Zang, J., Hillis, A., Morgan, G., Plummer, A., 2014. Numerical investigation of wave-structure interaction using OpenFOAM. Ocean Eng. 88, 91–109.

Collins, I., Hossain, M., Dettmer, W., Masters, I., 2021. Flexible membrane structures for wave energy harvesting: A review of the developments, materials and computational modelling approaches. Renew. Sustain. Energy Rev. 151, 111478.

Courant, R., Friedrichs, K., Lewy, H., 1928. Über die partiellen Differenzengleichungen der mathematischen Physik. Math. Ann. 100, 32–74.

Cross, R., 1967. Tsunami surge forces. J. Waterw. Harb. Div. 93 (4), 201–234.

Dawson, D., Shaw, J., Gehrels, W.R., 2016. Sea-level rise impacts on transport infrastructure: The notorious case of the coastal railway line at Dawlish, England. J. Transp. Geogr. 51, 97–109.

Degroote, J., 2013. Partitioned simulation of fluid-structure interaction. Arch. Comput. Methods Eng. 20 (3), 185–238.

Di Paolo, B., Lara, J.L., Barajas, G., Losada, I.J., 2021. Wave and structure interaction using multi-domain couplings for Navier-Stokes solvers in OpenFOAM®. Part I: Implementation and validation. Coast. Eng. 164, 103799.

Didier, E., Neves, D., Martins, R., Neves, M., 2014. Wave interaction with a vertical wall: SPH numerical and experimental modeling. Ocean Eng. 88, 330–341.

Erbisti, P., 2014. Design of Hydraulic Gates. Balkema, Lisse, Netherlans.

Evers, F.M., Heller, V., Hager, W.H., Boes, R.M., 2019. Landslide-generated impulse waves in reservoirs: Basics and computation. In: Boes, R. (Ed.), VAW-Mitteilung 254, 2nd ed. ETH Zurich, Zurich.

Ferziger, J.H., 1987. Simulation of incompressible turbulent flows. J. Comput. Phys. 69 (1), 1–48.

Fuchs, H., Hager, W.H., 2015. Solitary impulse wave transformation to overland flow. J. Waterw. Port Coast. Ocean Eng. 141 (5), 04015004.

Gibson, R.F., 2007. Principles of Composite Material Mechanics. CRC press, Florida.

Girfoglio, M., Quaini, A., Rozza, G., 2021. Fluid-structure interaction simulations with a LES filtering approach in solids4Foam. ArXiv Preprint ArXiv210208011.

He, G., Kashiwagi, M., 2012. Numerical analysis of the hydroelastic behavior of a vertical plate due to solitary waves. J. Mar. Sci. Technol. 17 (2), 154–167.

Heller, V., Hager, W.H., Minor, H.-E., 2009. Landslide-generated impulse waves in reservoirs: Basics and computation. In: Boes, R. (Ed.), VAW-Mitteilung 211. ETH Zurich, Zurich.

Hess, F., Boes, R.M., Evers, F.M., 2023. Forces on a vertical dam due to solitary impulse wave run-up and overtopping. J. Hydraul. Eng. (In press).

Higuera, P., Lara, J.L., Losada, I.J., 2013. Realistic wave generation and active wave absorption for Navier-Stokes models: Application to OpenFOAM®. Coast. Eng. 71, 102–118.

Higuera, P., Lara, J.L., Losada, I.J., 2014. Three-dimensional interaction of waves and porous coastal structures using OpenFOAM®. Part I: Formulation and validation. Coast. Eng. 83, 243–258.

Hirt, C.W., Nichols, B.D., 1981. Volume of fluid (VOF) method for the dynamics of free boundaries. J. Comput. Phys. 39, 201–225.

Hu, Z.Z., Greaves, D., Raby, A., 2016. Numerical wave tank study of extreme waves and wave-structure interaction using OpenFOAM. Ocean Eng. 126, 329–342.

Hu, Z., Huang, L., Li, Y., 2022. Fully-coupled hydroelastic modelling of a deformable wall in waves. Coast. Eng. 179, 104245.

Huang, L., Li, Y., Benites, D., Windt, C., Feichtner, A., Tavakoli, S., Davidson, J., Paredes, R., Quintuna, T., Ransley, E., Colombo, M., Li, M., Cardiff, P., Tabor, G., 2022. A review on the modelling of wave-structure interactions based on OpenFOAM. OpenFOAM J. 2, 116–142.

Huang, C., Zhang, D., Si, Y., Shi, Y., Lin, Y., 2018. Coupled finite particle method for simulations of wave and structure interaction. Coast. Eng. 140, 147–160.

Jacobsen, N.G., Fuhrman, D.R., Fredsøe, J., 2012. A wave generation toolbox for the open-source CFD library: OpenFOAM. Internat. J. Numer. Methods Fluids 70 (9), 1073–1088.

Jasak, H., 1996. Error Analysis and Estimation for the Finite Volume Method with Applications to Fluid Flows (Ph.D. thesis). Imperial College of Science, Technology and Medicine, London.

Khayyer, A., Gotoh, H., Falahaty, H., Shimizu, Y., 2018. An enhanced ISPH-SPH coupled method for simulation of incompressible fluid-elastic structure interactions. Comput. Phys. Comm. 232, 139–164.

Khayyer, A., Tsuruta, N., Shimizu, Y., Gotoh, H., 2019. Multi-resolution MPS for incompressible fluid-elastic structure interactions in ocean engineering. Appl. Ocean Res. 82, 397–414.

Kimmoun, O., Malenica, S., Scolan, Y.M., 2009. Fluid structure interactions occuring at a flexible vertical wall impacted by a breaking wave. In: The Nineteenth International Offshore and Polar Engineering Conference. pp. 308–315.

Krautwald, C., von Häfen, H., Niebuhr, P., Vögele, K., Stolle, J., Schimmels, S., Schürenkamp, D., Sieder, M., Goseberg, N., 2022. Collapse processes and associated loading of square light-frame timber structures due to bore-type waves. Coast. Eng. 104178.

Kumar, P., Yang, Q., Jones, V., McCue-Weil, L., 2015. Coupled SPH-FVM simulation within the openFOAM framework. Procedia IUTAM 18, 76–84.

Lagoun, M.S., Benalia, A., Benbouzid, M.E.H., 2010. Ocean wave converters: State of the art and current status. In: 2010 IEEE International Energy Conference. pp. 636–641.

Larsen, B.E., Fuhrman, D.R., 2019. Full-scale CFD simulation of tsunamis. Part 1: Model validation and run-up. Coast. Eng. 151, 22–41.

Launder, B., Spalding, D., 1974. The numerical computation of turbulent flows. Comput. Methods Appl. Mech. Engrg. 3 (2), 269–289.

Laya, E.J., Connor, J.J., Sunder, S.S., 1984. Hydrodynamic forces on flexible offshore structures. J. Eng. Mech. 110 (3), 433–448.

Li, Y., Raichlen, F., 2003. Energy balance model for breaking solitary wave runup. J. Waterw. Port Coast. Ocean Eng. 129 (2), 47–59.

Liao, K., Hu, C., Sueyoshi, M., 2015. Free surface flow impacting on an elastic structure: Experiment versus numerical simulation. Appl. Ocean Res. 50, 192–208.

Linton, D., Gupta, R., Cox, D., van de Lindt, J., Oshnack, M.E., Clauson, M., 2013. Evaluation of tsunami loads on wood-frame walls at full scale. J. Struct. Eng. 139 (8), 1318–1325.

Liu, M., Zhang, Z., 2019. Smoothed particle hydrodynamics (SPH) for modeling fluid-structure interactions. Sci. China Phys. Mech. Astron. 62 (8), 984701.

Lo, H.-Y., Park, Y.S., Liu, P.L.-F., 2013. On the run-up and back-wash processes of single and double solitary waves - An experimental study. Coast. Eng. 80, 1–14.

Mai, T., Mai, C., Raby, A., Greaves, D.M., 2020. Hydroelasticity effects on water-structure impacts. Exp. Fluids 61 (9), 1–19.

Mallayachari, V., Sundar, V., 1995. Standing wave pressures due to regular and random waves on a vertical wall. Ocean Eng. 22 (8), 859–879.

Miche, M., 1951. Le pouvoir réfléchissant des ouvrages maritimes exposés à l'action de la houle. Ann. Ponts ChaussÉEs 121, 285–319.

Moan, T., 2018. Life cycle structural integrity management of offshore structures. Struct. Infrastruct. Eng. 14 (7), 911–927.
Mohammadi, S., Nilsson, H., Cardiff, P., Rundström, D., 2021. Fluid-structure interaction on a fixed fan blade. In: The 16th OpenFOAM Workshop.
Morison, J., Johnson, J., Schaaf, S., 1950. The force exerted by surface waves on piles. J. Pet. Technol. 2 (5), 149–154.
Müller, D.R., 1995. Auflaufen und Überschwappen von Impulswellen an Talsperren (Ph.D. thesis no. 24650). ETH Zurich, Zurich.
O'Connor, J., Rogers, B.D., 2021. A fluid-structure interaction model for free-surface flows and flexible structures using smoothed particle hydrodynamics on a GPU. J. Fluids Struct. 104, 103312.
OpenFOAM extension, 2016. URL: https://sourceforge.net/u/hjasak/foam-extend-4.0/ci/master/tree/ accessed: 5 March 2023.
Peregrine, D.H., 2003. Water-wave impact on walls. Annu. Rev. Fluid Mech. 35 (1), 23–43.
Rao, C., Zhang, Y., Wan, D., 2017. Numerical simulation of the solitary wave interacting with an elastic structure using MPS-FEM coupled method. J. Mar. Sci. Appl. 16 (4), 395–404.
Rege, K., Hjertager, B.H., 2017. Application of foam-extend on turbulent fluid-structure interaction. In: IOP Conference Series: Materials Science and Engineering, Vol. 276. 012031.
Romano, A., Lara, J.L., Barajas, G., Di Paolo, B., Bellotti, G., Di Risio, M., Losada, I.J., De Girolamo, P., 2020. Tsunamis generated by submerged landslides: Numerical analysis of the near-field wave characteristics. J. Geophys. Res.: Oceans 125 (7), e2020JC016157.
Sainflou, M., 1928. Essai sur les digues maritimes verticales. Ann. Ponts Et Chaussees 98, 5–48.
Sotiropoulos, F., Yang, X., 2014. Immersed boundary methods for simulating fluid-structure interaction. Prog. Aerosp. Sci. 65, 1–21.
Sun, P., Touzé, D.L., Zhang, A.-M., 2019. Study of a complex fluid-structure dam-breaking benchmark problem using a multi-phase SPH method with APR. Eng. Anal. Bound. Elem. 104, 240–258.
Timoshenko, S., 1983. History of Strength of Materials: With a Brief Account of the History of Theory of Elasticity and Theory of Structures. Courier Corporation, New York.
Tuković, Z., Karač, A., Cardiff, P., Jasak, H., Ivanković, A., 2018. OpenFOAM finite volume solver for fluid-solid interaction. Trans. FAMENA 42, 1–31.
Ursell, F., Dean, R.G., Yu, Y., 1960. Forced small-amplitude water waves: A comparison of theory and experiment. J. Fluid Mech. 7 (1), 33–52.
van Veelen, T.J., Karunarathna, H., Reeve, D.E., 2021. Modelling wave attenuation by quasi-flexible coastal vegetation. Coast. Eng. 164, 103820.
von Häfen, H., Krautwald, C., Stolle, J., Bung, D.B., Goseberg, N., 2022. Overland flow of broken solitary waves over a two-dimensional coastal plane. Coast. Eng. 104125.
Weller, H., Tabor, G., Jasak, H., Fureby, C., 1998. A tensorial approach to computational continuum mechanics using object orientated techniques. Comput. Phys. 12, 620–631.
Xie, P., Chu, V.H., 2019. The forces of tsunami waves on a vertical wall and on a structure of finite width. Coast. Eng. 149, 65–80.
Yuan, Z., Huang, Z., 2015. Morison coefficients for a circular cylinder oscillating with dual frequency in still water: An analysis using independent-flow form of Morison's equation. J. Ocean Eng. Mar. Energy 1 (4), 435–444.
Zhang, G., Chen, X., Wan, D., 2019. MPS-FEM coupled method for study of wave-structure interaction. J. Mar. Sci. Appl. 18, 387–399.